Energy & Buildings 375 (2027) 118517

Contents lists available at ScienceDirect

Energy & Buildings

journal homepage: www.elsevier.com/locate/enbuild

Comprehensive modelling of exhaust air heat pumps for residential applications under cooling operation ⋆

Roberto Sedoni [a], Marco Romani [b], William Monteleone [c], Fabian Ochs [c], Diego Angeli [a,d,*], Paolo E. Santangelo [a,d]

[a] Dipartimento di Scienze e Metodi dell'Ingegneria, Università degli Studi di Modena e Reggio Emilia, Via Amendola 2, Reggio Emilia, 42122, Italy
[b] Zehnder Group – Competence Center Campogalliano, Via G. di Vittorio 6, Campogalliano, 41011, Italy
[c] University of Innsbruck, Unit of Energy Efficient Building, Department of Structural Engineering and Material Sciences, Technikerstraße 13, Innsbruck, 6020, Austria
[d] Centro Interdipartimentale En&Tech, Università degli Studi di Modena e Reggio Emilia, Piazzale Europa 1, Reggio Emilia, 42124, Italy

ARTICLE INFO

Keywords:
Exhaust air heat pump
Multifunctional ventilation unit
Physics-based model
Experimental validation
Cooling operation
Heat and energy recovery

ABSTRACT

Decarbonization of the building sector calls for more efficient heating, cooling, and ventilation solutions. Exhaust air heat pumps, which combine heat or enthalpy recovery and exhaust-to-supply air heat pump operation, offer a promising approach for low-energy buildings, but their performance depends on complex interactions and accurate prediction requires advanced numerical modeling and experimental validation. In this study, a high-fidelity digital model of an exhaust air heat pump is presented and validated under cooling operation through a dedicated experimental campaign. The model integrates detailed physics-based representations of all major components and of the onboard control logic, enabling accurate prediction of unit behavior. A comparison of the simulation results with experimental measurements across the full cooling operating range, including both full- and partial-load conditions, showed that overall performance indicators were predicted within ±10% across all tested conditions. The validated model was subsequently employed to explore operating scenarios and control strategies beyond the experimental campaign that still require investigation. Specifically, the analysis assessed the impact, on overall system-level performance, of the integration of an auxiliary outdoor-to-exhaust fan, the heat recovery strategy and the heat recovery bypass fraction, in on-design and off-design conditions. The analysis revealed the need to pursue a trade-off between maximizing system energy efficiency and ensuring the fulfillment of the required cooling capacity, highlighting how design and control choices can substantially influence overall system performance. These findings demonstrate the potential of digital models to advance the understanding, optimization, and operation of next-generation Heating, Ventilation and Air Conditioning systems in low-energy buildings.

1. Introduction

1.1. Background

In modern residential buildings with highly airtight envelopes, maintaining indoor air quality requires a constant and controlled exchange of indoor and outdoor air [1,2]. For energy efficiency reasons, this is typically achieved with Mechanical Ventilation with Heat Recovery (MVHR) systems [3], which recover a significant fraction of heat or enthalpy (heat and moisture) from the exhaust stream. While PassivHaus certified buildings can often meet comfort requirements with minimal reliance on active climatization (e.g., thermal load ≤10 W m^{-2}) [4], most new or renovated dwellings still require a modest but non-negligible active thermal conditioning, which is typically provided by air-to-air heat pumps due to their low cost, limited invasiveness, and ease of installation [5,6]. These features make them suitable for both new constructions and retrofit applications, including historic or heritage buildings where conservation rules limit the use of more efficient but more intrusive systems such as air-to-water or water-to-water heat pumps coupled with radiant systems. When the cooling (or heating) load is low, typically ranging from 20 to 40 W m^{-2}, and an MVHR system is already present, integrating an exhaust-to-supply air heat pump into the ventilation circuit—a configuration known as Exhaust Air Heat Pump (EAHP) or Multifunctional Balanced Ventilation (MFRBV) unit—offers a

⋆ This paper is a part of the special issue 'VSI: ENB_Building communities'.

* Corresponding author at: Dipartimento di Scienze e Metodi dell'Ingegneria, Università degli Studi di Modena e Reggio Emilia, Via Amendola 2, Pad. Buccola, Reggio Emilia, 42122, Italy.
E-mail address: diego.angeli@unimore.it (D. Angeli).

https://doi.org/10.1016/j.enbuild.2026.118517
Received 31 July 2026; Received in revised form 20 October 2026; Accepted 10 November 2026
Available online 14 November 2026
0378-7788/© 2026 The Authors. Published by Elsevier B.V. This is an open access article under the CC BY-NC-ND license (http://creativecommons.org/licenses/by-nc-nd/4.0/).

Nomenclature

Latin letters

A	area [m^2]
C	heat capacity rate [$W\,K^{-1}$]
CL	cooling load [W]
D_h	hydraulic diameter [m]
H	thickness [m]
L	length [m]
M	mass [kg]
PC	power consumption [W]
R	specific gas constant [$J\,kg^{-1}\,K^{-1}$]
RH	relative humidity [%]
T	temperature [K]
U	overall heat transfer coefficient [$W\,m^{-2}\,K^{-1}$]
V	volume [m^3]
W	humidity ratio [–]
W_s	saturation humidity ratio [–]
c_{wall}	wall specific heat [$J\,kg^{-1}\,K^{-1}$]
c_p	specific heat at constant pressure [$J\,kg^{-1}\,K^{-1}$]
f	Darcy friction factor [–]
h	specific enthalpy [$J\,kg^{-1}$]
k	thermal conductivity [$W\,m^{-1}\,K^{-1}$]
$\dot{m}$	mass flow rate [$kg\,s^{-1}$]
Nu	Nusselt number [–]
NTU	Number of Transfer Units [–]
p	pressure [Pa]
Pr	Prandtl number [–]
$\dot{Q}$	heat flow rate [W]
Re	Reynolds number [–]
t	time [s]
u	specific internal energy [$J\,kg^{-1}$]
x	vapor quality [–]
x_w	specific humidity [–]
x_{ws}	specific saturation humidity [–]

Greek letters

α	heat transfer coefficient [$W\,m^{-2}\,K^{-1}$]
Δh_v	latent heat of evaporation [$J\,kg^{-1}$]
ϵ	effectiveness [–]
η	efficiency [–]
ν	specific volume [$m^3\,kg^{-1}$]
ϕ	phase multiplier [–]
Φ	total energy [W]
ρ	density [$kg\,m^{-3}$]
τ	time constant [s]
ω	rotational speed [rpm]

Super/Subscripts

SL	saturated liquid
SV	saturated vapor
V	volume
avg	average
c	condensation
ch	channel
$count$	counter-flow
$cond$	condensed water
$cross$	cross-flow
dry	dry air
e	evaporation
eff	effective
in	inlet
$meas$	measured
mem	membrane
out	outlet
R	throat
s	sensible
sim	simulated
std	steady-state
sys	overall system
x	moisture
vap,t	vapor transfer
w	water

Abbreviations

2P	Refrigerant
EAHP	Exhaust Air Heat Pump
ERV	Energy Recovery Ventilation
ETA	Extract Air
EXH	Exhaust Air
HVAC	Heating Ventilation and Air Conditioning
HP	Heat Pump
HRV	Heat Recovery Ventilation
MA	Moist Air
MFRBV	Multifunctional Balanced Ventilation for residential
MPC	Model Predictive Control
MVHR	Mechanical Ventilation with Heat Recovery
ODA	Outdoor Air
OEA	Outdoor to Exhaust Air
PEXH	Post-Exhaust Air
PSUP	Post-Supply Air
SUP	Supply Air

technically and economically viable solution [7,8]. Although internally complex, an EAHP reduces infrastructural complexity by combining air renewal and thermal conditioning into a single packaged unit, which avoids parallel HVAC systems and lowers on-site installation efforts. However, the balanced and constant airflow imposed by the MVHR often forces the heat pump (HP) to operate under suboptimal conditions, making performance highly sensitive to airflow magnitude, air conditions, and control strategy [9].

1.2. Literature survey

Recent studies on EAHPs have shown that performance improvements are achievable not only through component upgrades but also through a fundamental redesign of system architectures. A primary bottleneck for conventional EAHPs operating in cooling mode is the inadequate exhaust airflow through the condenser, which limits heat transfer and increases condensing temperature. Research has therefore focused on architectural enhancements aimed at decoupling thermal loads, optimizing airflow, and maximizing heat recovery.

Regarding load decoupling, Cao et al. [10] proposed a novel packaged outdoor air dehumidifier featuring a decoupled subcooler and condenser, achieving an energy efficiency ratio (EER) of 3.65 and a dehumidification capacity of 78.2 kg/day under rated conditions. Similarly, Liang et al. [11] integrated a direct expansion dehumidification unit with a membrane-based total heat exchanger, using exhaust air to precool and dehumidify fresh air; this reduced energy consumption while yielding a 50% higher dehumidification rate and an EER twice that of conventional setups.

To further mitigate the exhaust airflow bottleneck, alternative strategies focus on redistributing the condensation load or recovering rejected heat. By dividing the heat rejection process, the thermal load on the primary exhaust condenser is significantly alleviated. As an ex-

ample of that, Zhang et al. [12] developed a configuration featuring an additional dedicated outdoor condenser operating in parallel. By optimizing the refrigerant mass flow ratio between the two condensers, this system achieved an EER of 3.3 under 35°C ambient conditions. Parallel-loop architectures have shown further gains: Li et al. [13] reported EER improvements up to 64.05% with peak capacities exceeding 8 kW, and Jia et al. [14] achieved EERs around 7 in highly optimized setups. Beyond merely dividing the load across air-cooled heat exchangers, redefining the heat sink itself can drastically improve system efficiency. Notably, Li et al. [9] developed a high-efficiency EAHP integrating an indirect evaporative cooler with an evaporative condenser. Their prototype yielded cooling capacity and EER improvements of 53% and 135%, respectively, relative to conventional systems. Finally, rather than simply rejecting heat to the environment, system architectures can be designed to actively recover it. For instance, capturing condenser waste heat for domestic hot water production maximizes the utilization of rejected thermal energy. Empirical evidence supports this integration; Thalfeldt et al. [15] recorded seasonal energy efficiency ratios (SEER) between 3.55 and 3.59 for such systems, while Sikder et al. [16] demonstrated the successful recovery of up to 4.28 kW of thermal energy.

In parallel with architectural modifications, advanced control strategies and digital twins represent a powerful complementary, enhancement pathway. Model Predictive Control (MPC) has emerged as a leading solution: Guo et al. [17], Tang et al. [18], and Si et al. [19] demonstrated its potential to improve efficiency, flexibility, and comfort, in EAHP systems, while highlighting its dependence on accurate dynamic models. To address this challenge, digital twins are increasingly being adopted. Data-driven approaches, such as the Gaussian Process Regression model developed by Ispir et al. [20], can achieve prediction errors below 7%. However, their reliability remains fundamentally constrained by dataset coverage and operational stability, leading to inherent struggles in accurately capturing highly nonlinear phenomena, such as evaporator frosting or coupled air-refrigerant dynamics [19,21]. In contrast, physics-based digital twins inherently embed conservation laws and fundamental thermodynamic principles. This structural advantage provides greater interpretability and robustness under variable operating conditions, making them more suitable for the design of innovative system configurations and advanced control strategies.

1.3. Motivation and objectives

Despite the growing relevance of EAHPs, comprehensive experimental characterizations of these systems remain scarce. Given the high costs associated with climatic chamber testing, a significant research gap persists regarding the availability of high-fidelity, laboratory-grade datasets obtained under realistic off-design conditions. This scarcity of data constrains both design refinement and the development of robust control strategies. Furthermore, the impact of specific architectural enhancements and control strategies on system-level performance has not been sufficiently quantified in the existing literature, especially under partial-load conditions. In particular, the effect of increasing the airflow rate across the HP outdoor coil through an auxiliary outdoor-to-exhaust air (OEA) fan, the influence of the recovery exchanger type, either enthalpy (ERV) or sensible-only (HRV), and the effect of bypassing the recovery exchanger have not been systematically assessed for such systems.

The novelty of this study lies in combining an extensive experimental campaign, reproducing summer conditions, with a physics-based digital model rigorously validated against the measured data. To ensure the direct relevance of the findings, the unit is tested under operating conditions (i.e., airflow rates and temperatures) representative of the residential sector. The validated model is then employed to systematically investigate these design and control scenarios under both full- and partial-load cooling conditions. Specifically, the research addresses three main questions: (i) does the use of an auxiliary outdoor-to-exhaust air fan, which increases the airflow rate across the HP outdoor coil, improve overall system performance?; (ii) does the system perform more effectively when coupled with an enthalpy or a sensible-only recovery exchanger?; (iii) does partial or full bypass of the recovery exchanger enhance overall system performance?

2. System description

The multifunctional ventilation unit investigated in this study is illustrated in Fig. 1. The system consists of a mechanical recovery ventilation unit coupled in series with a reversible exhaust-to-supply air heat pump.

In its standard configuration, the unit operates with balanced mass flow rates on both the indoor and outdoor sides. It includes a supply air (SUP) and extract air (ETA) stream, each handled by dedicated fans (components 2 and 3), and a recovery exchanger (component 1). Depending on the specific operating scenario, this exchanger can be configured as either a sensible heat recovery (HRV) or a energy recovery (ERV) core, enabling heat or enthalpy (heat and moisture) transfer between the extract and outdoor air streams. The system features a bypass mechanism—indicated by the dashed lines surrounding the heat recovery exchanger in Fig. 1—which permits the partial or full bypass of the recovery stage. A heat pump circuit is arranged downstream of the ventilation unit, including a compressor (component 12), a four-way reversing valve (component 13), an electronic expansion valve (component 14), and two finned-tube heat exchangers (components 10 and 11), which serve as the outdoor and indoor coils of the refrigeration cycle. An accumulator (not shown in Fig. 1) is included upstream of the compressor, on the suction line, to prevent liquid refrigerant from entering the compressor and potentially damaging it.

To evaluate the effects of increasing the airflow across the outdoor coil, the unit can incorporate an auxiliary outdoor-air recirculation loop (OEA), highlighted in red in Fig. 1. When this arrangement is active, a dedicated fan (component 4) draws an auxiliary stream of outdoor air and mixes it with the exhaust air discharged by the ventilation unit. The resulting mixture is then conveyed to the outdoor-side heat exchanger (component 10). By increasing the total air mass flow rate and altering the temperature and humidity of the air entering the coil, the additional OEA recirculation loop modifies the boundary conditions experienced by the refrigerant circuit. This functionality is specifically intended to stabilize the operation of the heat pump and enhance its performance under unfavorable conditions, including very low or very high outdoor temperatures as well as reduced ventilation flow rates. To contain noise, the OEA fan speed is subject to an upper limit, which constrains the maximum airflow rate through the recirculation loop.

The heat pump is equipped with a dedicated control system designed to ensure both efficiency and safe operation. Three temperature sensors, factory-installed on the refrigeration circuit, are used for this purpose: one on each heat exchanger to measure the condensation and evaporation temperatures, and one at the compressor discharge to monitor the discharge temperature. These measurements are used to implement a low-level protection logic that prevents the compressor from operating outside its envelope curve. In particular, both the condensation and discharge temperatures must remain below predefined thresholds in heating and cooling modes, in addition the evaporation temperature in cooling mode must not drop excessively to avoid coil frosting. Furthermore, a high-level protection logic dynamically limits the maximum compressor frequency as a function of air temperature conditions and ventilation flow rate. This additional layer of protection is specifically intended to prevent the system from frequently triggering the low-level protection logic, thereby ensuring more stable and reliable operation. The same temperature measurements are also used to regulate the electronic expansion valve, which indirectly controls refrigerant superheat and ensures proper refrigerant distribution within the evaporator.

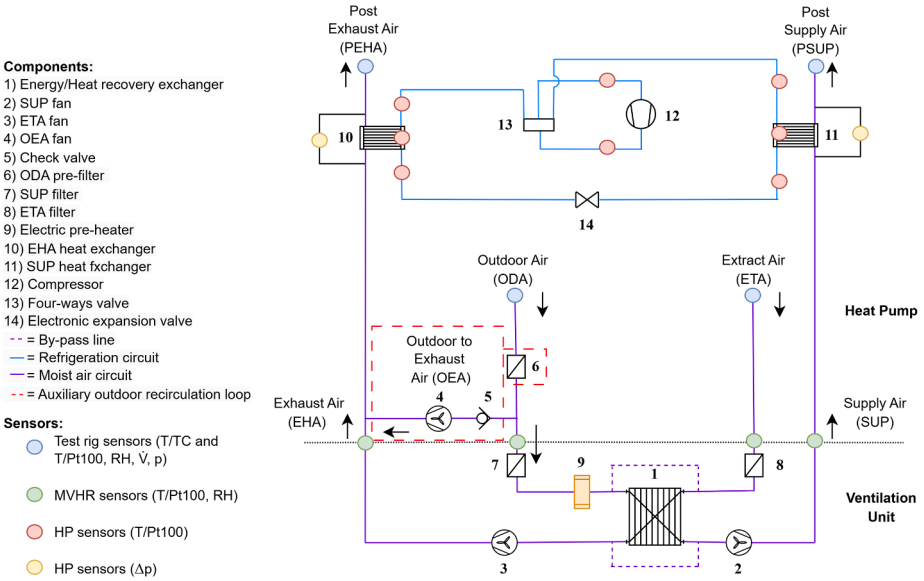

Fig. 1. Full schematic of the HVAC unit investigated.

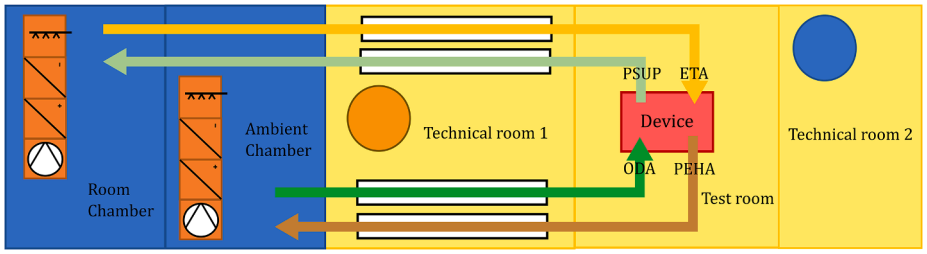

Fig. 2. Full schematic of the laboratory setup.

3. Experiments

3.1. Test rig

The experimental campaign was carried out at the *Kompakt-geräteprüfstand* laboratory of the University of Innsbruck. The core of the testing facility, illustrated in Fig. 2, features a central test room, two climatic chambers and two technical rooms. The unit under test is installed in the Test room (see Fig. 2), a thermally stable and acoustically treated room connected to two climatic chambers that are used to simulate indoor and outdoor environments. The Room chamber (see Fig. 2) provides up to 8.0 kW of cooling capacity at 21°C and 3.5 kW of heating capacity. The Ambient chamber (see Fig. 2) delivers up to 8.0 kW of cooling capacity at 2°C (6.5 kW at −7°C) and 9.4 kW of heating capacity.

Temperature and humidity inside the two climatic chambers are controlled by dedicated PI-PID in cascade controllers, which allow the inlet conditions of the unit under test to be maintained within ±0.05,°C and ±2, % RH. Volumetric flow rates are measured using calibrated orifice plates. Humidity is monitored by capacitive probes placed downstream of the unit outlets, where the air is sufficiently mixed to ensure reliable sampling. These sensors were selected for their fast response time and were recalibrated against a certified high-precision dew point sensor prior to the experimental campaign to ensure high accuracy. The average cross-sectional air temperature at each inlet and outlet section is measured with five sensors: four type-K thermocouples distributed circumferentially away from the walls, combined with one central PTC thermistor.

Auxiliary fans installed in each duct are used to set the static pressure at the unit openings, and controlled via PID loops. Power meters are used to continuously monitor the electrical consumption of the unit under test.

The complete list of sensors and their measurement accuracies is reported in Table 1.

3.2. Unit

The unit analyzed in the experimental campaign corresponds to the standard configuration described in Section 2 and equipped with an enthalpy recovery exchanger. Details on its main components, as declared by the manufacturer, are summarized in Table 2.

To achieve a comprehensive mapping of unit operation, additional onboard instrumentation was integrated, as illustrated in Fig. 1. Eight Refrigerant-side resistance thermometers (red) were mounted on the external surface of the copper tubes with conductive paste and insulated with 10 mm of flexible elastomeric foam. These sensors were placed at the inlets and outlets of the condenser and evaporator, as well as at the compressor suction and discharge. To obtain representative condensation and evaporation temperatures, further probes were mounted on central return bends of the heat exchangers, in positions shielded from the air stream, where the tube wall temperature closely reflects the mean refrigerant saturation temperature (Fig. 3). These sensors were deliberately located near the unit built-in probes used by the internal control logic, ensuring consistency between experimental data and the reference signals of the machine (Table 3).

Two air-side differential pressure sensors (yellow) were installed across the condenser and evaporator channels to quantify pressure losses. Finally, four RH/T sensors (green) were positioned at the inlets and outlets of the ventilation unit, centrally within the ducts to avoid wall effects, enabling accurate characterization of the air entering the

Table 1
Measurement devices and accuracies of the test rig sensors.

Measured value	SI unit	Device	Accuracy
Temperature	°C	1 × Pt100 4-wire with NI 9217; 4 × type-K thermocouples with NI 9213	Pt100: ±0.05 °C; TC: ±0.10 °C
Temperature/Relative humidity	°C, %	Pt100 and capacitive humidity sensors (E + E EE210)	T: ±0.10 °C; RH: ±1.5%
Volume flow	m^3/h	FläktWoods MR; Huba Control 699	±5.0%
Absolute pressure	Pa	THIES Clima Barogeber	±25 Pa
Differential pressure	Pa	Huba Control 699	±2 Pa
Electrical power consumption	W	Iskra MT 400	±0.5%

Table 2
Details on components of the tested unit.

Ventilation unit with heat recovery	
Enthalpy exchanger	
Type	Counter-flow, diamond-shaped multi-plate
Heat recovery rate[a]	90%
Humidity recovery[a]	75%
Specific electric power[a]	0.25 Wh/m^3
Ventilators	
Product	EC motors, backward-curved centrifugal, 115 W
Filters	
ODA-SUP side	ISO Coarse >65% (G4)
ETA-EHA side	ISO ePM1 >55% (F7)
Reversible air-to-air heat pump	
Airflow range	200-400 m^3/h
Refrigerant	R32
Fill charge	0.65 kg
Compressor	
Type	Rotary
Supply voltage	230 V, 50 Hz, single-phase
Maximum power consumption	1100 W
Current draw	4.87 A
Electronic expansion valve	
Type	Bidirectional
Finned-tube heat exchangers	
Outer heat transfer area	6.15 m^2
Inner heat transfer area	0.364 m^2

[a] Passive House certified data.

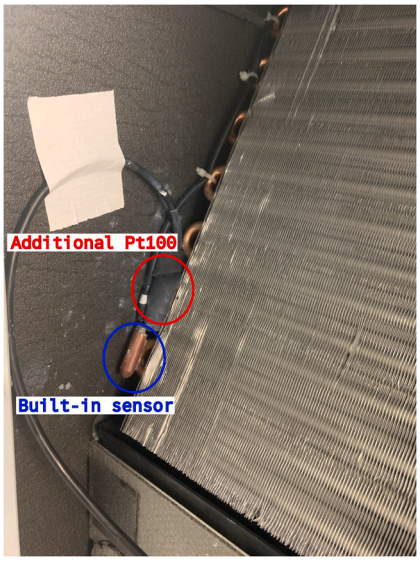

Fig. 3. Installation of refrigerant-side temperature sensor on the coil, for saturation temperature measurement.

heat pump. No additional insulation was applied to the unit beyond the factory configuration, in order to preserve realistic operating conditions. The casing of the unit was already insulated, as was most of the refrigerant circuit; only the compressor body and a short section of the discharge line, from the compressor outlet to the four-way valve, were left exposed. Maintaining this layout ensured that the tests remained representative of real installations. A full overview of the experimental testbench is shown in Fig. 4.

3.3. Test procedure

The adopted test matrix is represented in Fig. 5. The testing methods and operating conditions were selected in accordance with the UNI EN 16573:2017 standard [22]. The Ambient chamber, representing outdoor conditions, was set to $T_{ODA} = 27, 30$ and 35°C with a fixed relative humidity of 50%, while the Room chamber, representing indoor conditions, was maintained at 22 °C and 50% RH. This indoor condition, although lower than the conventional summer cooling condition (e.g., 26°C), was selected to guarantee an adequate temperature lift across the system under all tested conditions. In particular, at an outdoor temperature of 27°C, a standard indoor condition would result in an extremely small temperature difference between the source and sink reservoirs. This, consequently, would lead to an unrealistically low pressure ratio and potentially unstable compressor operation.

The test matrix was designed to provide a comprehensive mapping of the unit operating domain in cooling mode, varying both the outdoor temperature and the airflow rate. For each outdoor condition, three temperature setpoints (T_{set}) of 10, 15, and 20°C were initially targeted, representing the minimum, an intermediate, and the maximum allowable temperature settings of the unit. However, due to operational constraints, a specific test point was considered unfeasible, and therefore not tested, whenever the compressor had al-



Fig. 4. Overview of the experimental testbench.

Table 3
Measurement devices and accuracies of the additional sensors placed in the unit.

Measured value	SI unit	Device	Accuracy
Temperature	°C	Pt100 4-wire with NI 9217	±0.05 °C
Temperature/Relative humidity	°C, %	Pt100 and capacitive humidity sensors (KFFT/M-X/S)	T: ±0.30 °C; RH: ±2%
Differential pressure	Pa	Huba Control 699	±2 Pa

ready reached its maximum or minimum frequency at the preceding temperature setpoint. For example, at $\dot{V} = 200\ \mathrm{m^3h^{-1}}$ and $T_{\mathrm{ODA}} = 35\ °\mathrm{C}$, the $T_{\mathrm{set}} = 10°\mathrm{C}$ condition was skipped because the compressor was already operating at maximum speed for $T_{\mathrm{set}} = 15°\mathrm{C}$. Conversely, at the same airflow rate but $T_{\mathrm{ODA}} = 30\ °\mathrm{C}$, the $T_{\mathrm{set}} = 20°\mathrm{C}$ condition was excluded because the minimum speed was already reached at $T_{\mathrm{set}} = 15°\mathrm{C}$. Each $(T_{\mathrm{ODA}}, T_{\mathrm{set}})$ combination was tested at three values of ventilation flow rate, $\dot{V} = 200, 300$ and $400\ \mathrm{m^3h^{-1}}$, thus defining the complete test matrix shown in Fig. 5, where green points indicate tested conditions and red points unfeasible (not tested) conditions.

Data logging was initiated only after the ventilation unit reached steady-state, at which point the heat pump was switched on. Each operating condition was then maintained for approximately one hour, which proved sufficient for both subsystems to stabilize.

To obtain a consistent mapping of fans power consumption, a constant external pressure difference of 50 Pa was applied to each duct relative to the ambient.

In order to have validation data for the MVHR/HRV model, complementary measurements were performed on the ventilation subsystem alone, with the heat pump switched off. This configuration was tested at $T_{\mathrm{ODA}} = 27,\ 30$, and 35°C with flow rates ($\dot{V}$) of 200, 300, and $400\ \mathrm{m^3h^{-1}}$. Additionally, six measurements from previous campaigns were available for the MVHR/ERV variant at $\dot{V} = 150\ \mathrm{m^3h^{-1}}$ under identical outdoor conditions. For these tests, the ambient chamber relative humidity was fixed at 50%, while the room chamber was maintained at 22 °C and 50% RH. The full recorded experimental dataset has been made available in a public repository [23].

4. Model

The modeling framework adopts a system-level approach that combines lumped and distributed parameter representations, with the overall model assembled according to the system configuration presented in Fig. 1. The two finned-tube heat exchangers in the HP are discretized

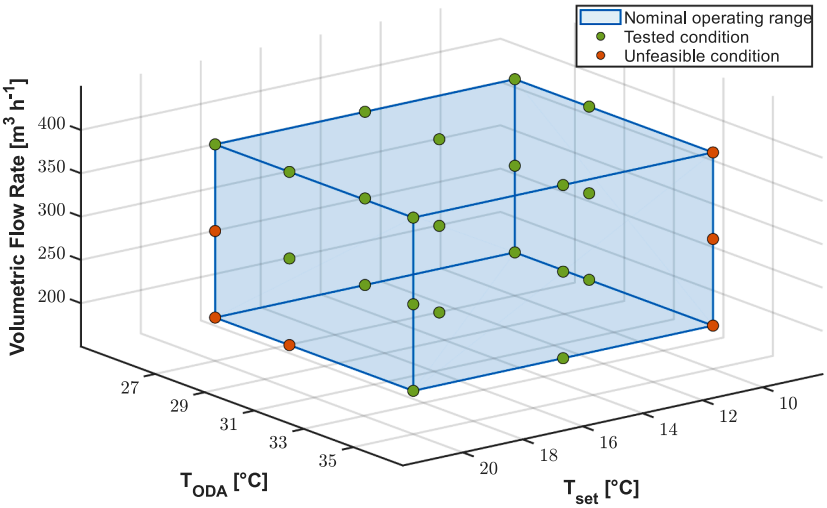

Fig. 5. Test matrix for the MFRBV/ERV unit.

into multiple control volumes to resolve local gradients, whereas other components of the network are modeled as single control volumes to balance accuracy and computational cost.

The conservation equations of mass and energy are formulated for each component and assembled into a global differential-algebraic system solved iteratively at each time step.

The model is implemented using the Simscape toolbox in MATLAB/Simulink® [24] environment, which manages the numerical solution and implementation of the control logic of the unit.

The governing equations of the heat exchangers and of the accumulator are formulated in transient form, in accordance with the charge-based approach adopted on the refrigerant side. In this approach, the refrigerant charge is set by the initial pressure and specific internal energy assigned to the control volumes of these components, which determine the refrigerant mass initially contained in each of them. The total charge is then conserved throughout the simulation, while its distribution among the components varies with the evolving system state and boundary conditions. Unlike conventional steady-state models, in which the condensation pressure or the subcooling is prescribed, the pressure levels are therefore free to adjust, and the resulting operating conditions reflect the actual refrigerant charge of the unit. This makes the formulation more general and allows off-design conditions to be predicted more reliably. Likewise, the air-side model of the heat recovery exchanger, developed as a custom component, accounts for air mass and energy storage and for the thermal capacity of the exchanger walls. This provides a formulation consistent with the rest of the network and prevents purely algebraic couplings with the adjacent air-side control volumes, improving the numerical robustness of the solution. The same formulation also allows the control logic of the unit to be active in the control-driven analysis, where the steady-state conditions are not imposed but are reached under the action of the controllers (e.g., compressor modulation and expansion valve regulation). Within the scope of the present study, the transient formulation is therefore employed purely as a means to compute the steady-state operating points, and both the model validation and subsequent analyses rely exclusively on steady-state conditions.

A comprehensive overview of the modeled components, distinguishing between custom-developed and pre-defined library blocks, is presented in Table 4.

4.1. Recovery heat exchanger

Since no model of the recovery exchanger is available in the standard Simscape libraries, this component was developed as a custom block based on established formulations, and its governing equations are reported below for completeness and reproducibility.

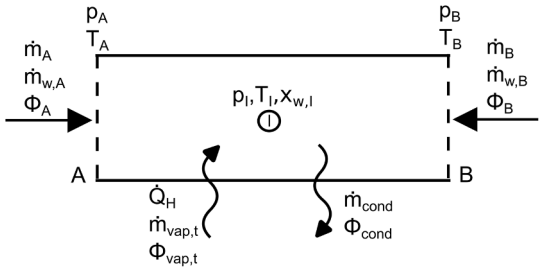

Fig. 6. Moist air.

4.1.1. Moist air control volume

The recovery exchanger is modeled with two moist-air control volumes (Fig. 6), one for each airflow side (EE and OS), each of volume V.

Wall condensation in the recovery exchanger is assumed to be negligible, given its rare occurrence under summer conditions in such components [28].

The internal moist air volume state is described by the three variables p_I, T_I, $x_{w,I}$ representing pressure, temperature and specific humidity respectively. Mass and water balances equations are [26]:

$$\left(\frac{1}{p_I}\frac{dp_I}{dt} - \frac{1}{T_I}\frac{dT_I}{dt}\right)\rho_I V + \frac{R_{dry} - R_w}{R_I}\left(\dot{m}_{w,net} - x_{w,I}\dot{m}_{net}\right) = \dot{m}_{net} \tag{1}$$

$$\frac{dx_{w,I}}{dt}\rho_I V + x_{w,I}\dot{m}_{net} = \dot{m}_{w,net} \tag{2}$$

here R_I is the specific mixture constant of the moist air volume. Instead, the energy conservation reads:

$$\rho_I(c_{p,I} - R_I)V\frac{dT_I}{dt} + (u_w - u_{dry})(\dot{m}_{w,net} - x_{w,I}\dot{m}_{net}) + u_I\dot{m}_{net} = \Phi_{net} \tag{3}$$

In Eqs. (1)–(3), and according to the positive flow direction shown in Fig. 6, the net flow rates are defined as:

$$\text{Total mass:} \quad \dot{m}_{net} = \dot{m}_A + \dot{m}_B - \dot{m}_{cond} + \dot{m}_{vap,t} \tag{4}$$

$$\text{Water mass:} \quad \dot{m}_{w,net} = \dot{m}_{w,A} + \dot{m}_{w,B} - \dot{m}_{cond} + \dot{m}_{vap,t} \tag{5}$$

$$\text{Energy:} \quad \Phi_{net} = \Phi_A + \Phi_B + \dot{Q}_H - \Phi_{cond} + \Phi_{vap,t} \tag{6}$$

Table 4
Description of the components in the model.

Component	Short description
Recovery exchanger	Custom-developed block.
Compressor	Custom-developed block.
Condenser/Evaporator	Custom-developed block described in [25].
Fans	Slight customization of the Flow Rate Source (MA) block from [26]. Fan affinity laws [27] are implemented to calculate rotational speed and power consumption.
Expansion valve	Pre-defined Local Resistance (2P) block from [26].
Accumulator	Pre-defined Receiver-Accumulator (2P) block from [26].
Air-side pressure losses	Pre-defined Flow Resistance (MA) block from [26].
Refrigerant-side pressure losses	Pre-defined Flow Resistance (2P) block from [26].

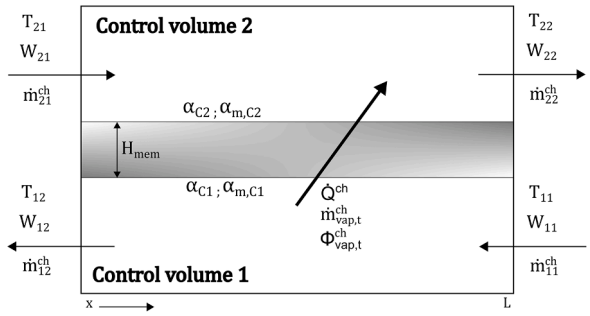

Fig. 7. Control volumes for the single-channel analysis.

Pressure losses are modeled using the semi-empirical relation:

$$p_A - p_B = \Delta p_{loss} \tag{7}$$

where $\dot{m}_{avg} = (\dot{m}_A - \dot{m}_B)/2$ denotes the average mass flow rate through the component, and $\Delta p_{loss} = a|\dot{m}_{avg}|\dot{m}_{avg} + b\dot{m}_{avg}$ is the empircal pressure loss of the component. Here a and b are empirical coefficients provided in the manufacturer's datasheet. With this definition, Δp_{loss} assumes a positive or negative value depending on the sign of $\dot{m}_{avg}$. This ensures that the resulting term is always applied with a physically consistent sign when introduced into Eq. (7). To close the system of equations, an intermidiate pressure ($p_I = \frac{p_A + p_B}{2}$) is defined at the control volume node 'I'.

To avoid unphysical conditions during the cooling of the moist air volume in the simulation, such as relative humidity exceeding 100%, the excess water vapor is assumed to condensate in the bulk-flow and is then removed in liquid form from the control volume:

$$\dot{m}_{cond} = \begin{cases} 0 & x_{w,I} \le x_{ws,I}, \\ \dfrac{x_{w,I} - x_{ws,I}}{\tau_{cond}}\,\rho_I V & x_{w,I} > x_{ws,I}, \end{cases} \tag{8}$$

where τ_{cond} is the characteristic time constant of the condensation process, set to 0.001 s as proposed in our previous study [25]. The energy term associated with this condensed water is:

$$\Phi_{cond} = \dot{m}^V_{cond} h^V_{wl,cond} \tag{9}$$

which is subtracted in the net energy flow rate (Eq. (6)). Here, $h^V_{wl,cond}$ is the specific enthalpy of the condensed water in the bulk-flow, evaluated at the control volume temperature T_I.

4.1.2. Heat and moisture transfer

Heat and moisture transfer are evaluated with a single-channel (counter-flow) analysis (Fig. 7) and then scaled to the whole exchanger. In this framework, by convention, fluxes are taken positive from control volume 1 (C1) to control volume 2 (C2).

Sensible heat. Per channel, the ϵ–NTU method gives:

$$\dot{Q}^{ch} = \epsilon_s (\dot{m}^{ch} c_p)_{min} (T_{11} - T_{21}), \qquad \epsilon_s = \frac{1 - \exp[-NTU_s(1 - C_r)]}{1 - C_r \exp[-NTU_s(1 - C_r)]} \tag{10}$$

with $NTU_s = U_s A^{ch}/C_{\min}$ and $U_s A^{ch} = \left(\frac{1}{\alpha_{C1} A^{ch}} + \frac{H_{mem}}{k_{mem} A^{ch}} + \frac{1}{\alpha_{C2} A^{ch}}\right)^{-1}$.

Convective coefficients (α_{C1} and α_{C2}) are estimated with the correlation of Muzychka and Yovanovich [29], which accounts for laminar developing flows in non-circular ducts. Real boundary conditions lie between uniform wall temperature (UWT) and uniform wall flux (UWF), therefore both limits are considered, as suggested by Zhang et al. [30].

Moisture transfer. Analogously, the exchanged water vapor per channel is:

$$\dot{m}^{ch}_{vap,t} = \epsilon_x (\dot{m}^{ch}_{dry})_{min} (W_{11} - W_{21}), \qquad \epsilon_x = \frac{1 - \exp[-NTU_x(1 - R^*)]}{1 - R^* \exp[-NTU_x(1 - R^*)]} \tag{11}$$

with $NTU_x = U_x A^{ch}/\dot{m}_{\min}$ and $R^* = \frac{\dot{m}^{ch}_{\min}}{\dot{m}^{ch}_{\max}}$. The associated water vapor energy transfer is $\Phi^{ch}_{vap,t} = \dot{m}^{ch}_{vap,t} h_{vap,t}$ with $h_{vap,t}$ the specific enthaply of water vapor at $\overline{T}_{mem}$.

The overall mass transfer conductance $U_x A^{ch} = \left(\frac{1}{\alpha_{m,C1} A^{ch}} + \frac{H_{mem}}{P_{mem} A^{ch}} + \frac{1}{\alpha_{m,C2} A^{ch}}\right)^{-1}$ accounts for convective terms and membrane permeability P_m, modeled following [31–33] as function of the average relative humidity (derived from [34]) and average membrane temperature ($\overline{T}_{mem} = \frac{T_{wall,EE} + T_{wall,OS}}{2}$). Convective mass transfer coefficients ($\alpha_{m,C1}$ and $\alpha_{m,C3}$) are obtained through the Chilton–Colburn analogy [35].

In case of a heat recovery exchanger $\dot{m}_{vap,t}$ is directly set to 0, and moisture transfer is not computed.

Scaling and cross-flow integration. The total sensible heat ($\dot{Q}^{std}$) and moisture transfer ($\dot{m}_{vap,t}$, $\Phi_{vap,t}$) at steady-state are obtained by scaling the single-channel results ($\dot{Q}^{ch}$,$\dot{m}^{ch}_{vap,t}$,$\Phi^{ch}_{vap,t}$) with the total number of channels.

Since the recovery exchanger used in the analyzed system—as is often the case for this type of device—operates in a mixed cross–counter-flow configuration, assuming purely counter-flow or neglecting the cross-flow section would lead to significant errors. To account for this, following Siegele et al. [36], the cross-counter-flow effectiveness (ϵ^{cc}) is computed as a weighted average of the values obtained by considering the entire heat transfer area first in a counter-flow (ϵ^{count}) and then in a cross-flow arrangement (ϵ^{cross}):

$$\epsilon^{cc}_s = \frac{A_{count}\,\epsilon^{count}_s + A_{cross}\,\epsilon^{cross}_s}{A_{count} + A_{cross}}, \qquad \epsilon^{cc}_x = \frac{A_{count}\,\epsilon^{count}_x + A_{cross}\,\epsilon^{cross}_x}{A_{count} + A_{cross}} \tag{12}$$

here A_{count} and A_{cross} denote the surface areas in counter-flow and cross-flow configurations. This correction provides a simple yet accurate way to represent the mixed geometry of plate-type exchangers in system-level simulations.

Transient wall model. A two-node wall model is used to capture the transient behavior by splitting the wall into two thermal

masses (adjacent to EE and OS control volumes) that exchange heat conductively:

$$\frac{M_{wall}c_{wall}}{2}\frac{dT_{wall,EE}}{dt} = -\dot{Q}_{H,EE} - \dot{Q}^{std} \tag{13}$$

$$\frac{M_{wall}c_{wall}}{2}\frac{dT_{wall,OS}}{dt} = -\dot{Q}_{H,OS} + \dot{Q}^{std} \tag{14}$$

The terms $\dot{Q}_{H,EE}$ and $\dot{Q}_{H,OS}$ represent the convective heat exchange between the wall surface and the moist-air stream in each control volume:

$$\dot{Q}_{H,EE} = \alpha_{EE}\, A_{EE}\left(T_{wall,EE} - T_{EE}\right) \tag{15}$$

$$\dot{Q}_{H,OS} = \alpha_{OS}\, A_{OS}\left(T_{wall,OS} - T_{OS}\right) \tag{16}$$

with A_{EE}, A_{OS} the heat transfer area on the two sides, and α_{EE}, α_{OS} the equivalent heat transfer coefficients, evaluated as weighted averages of the coefficients in the counter-flow and cross-flow sections, in the same way as the equivalent effectiveness (Eq. (12)).

4.2. Compressor

The compressor is modeled using a quasi-steady lumped formulation, with compressor work defined as ($\dot{W}$):

$$\dot{W} = \dot{m}(h_{out} - h_{in}), \qquad h_{out} = h_{in} + \frac{h_{out,ise} - h_{in}}{\eta_{ise}} \tag{17}$$

where $h_{out,ise}$ is the isentropic outlet enthalpy.

The mass flow rate through the component is related to the displacement volume V_{disp} and the rotational speed ω as follows:

$$\dot{m} = \rho_{in} V_{disp} \omega \eta_v \tag{18}$$

A volumetric efficiency map, $\eta_v(pr, \omega)$, is derived from manufacturer data and linearly interpolated—without extrapolation—to cover the entire operating range. Conversely, the isentropic efficiency map, $\eta_{ise}(pr, \omega)$, is determined experimentally, as detailed subsequently.

To complete the compressor model, power consumption (PC) is evaluated using a standard 20-coefficient polynomial [37]:

$$\begin{aligned} PC = {} & C_1 + C_2 T_e + C_3 T_c + C_4 \omega + C_5 T_e T_c + C_6 T_e\, \omega + C_7 T_c\, \omega \\ & + C_8 T_e^2 + C_9 T_c^2 + C_{10}\omega^2 + C_{11} T_e T_c\, \omega + C_{12} T_e^2 T_c \\ & + C_{13} T_e^2 \omega + C_{14} T_e^3 + C_{15} T_e T_c^2 + C_{16} T_c^2 \omega + C_{17} T_c^3 \\ & + C_{18} T_e \omega^2 + C_{19} T_c \omega^2 + C_{20} \omega^3 \end{aligned} \tag{19}$$

with coefficients, $C_1 - C_{20}$, obtained from manufacturer data.

During the simulation routine, the compressor block receives as input a smoothed rotational speed signal, computed by the system control logic based on the current operating conditions. This control logic not only determines the speed setpoint for capacity regulation but also integrates several protection strategies to maintain the compressor within its operating envelope.

4.2.1. Heat loss correction

To achieve consistent agreement between measured and simulated discharge temperatures, an additional heat-loss term was introduced downstream of the ideal adiabatic compression process. This discrepancy was attributed to thermal losses through the compressor shell and the non-insulated section of the discharge line, which lowered the measured discharge temperature compared with the ideal prediction. To quantify this effect, dedicated measurements were carried out under steady summer conditions (Fig. 8), with the compressor body and discharge line additionally insulated using a 10 mm flexible elastomeric foam layer. From measurements in the insulated case, a lookup table of isentropic efficiency, as a function of pressure ratio (pr) and compressor speed (ω), was derived. Heat losses in the uninsulated configuration were then identified by matching measured and predicted discharge

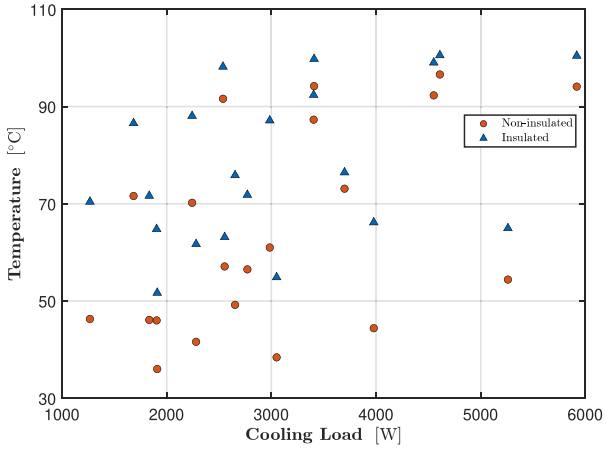

Fig. 8. Discharge temperatures recorded with the discharge line insulated and non-insulated.

temperatures based on the efficiency map. This led to the introduction of an empirical heat-loss term:

$$\dot{Q}_{loss} = K(pr, \omega)\dot{W}_{comp} \tag{20}$$

where $K(pr, \omega)$ is the heat-loss factor, tabulated and linearly interpolated across the domain.

The data in Fig. 8 and in the next sections are presented as a function of the Cooling Load (CL), which represents the total cooling capacity that the unit must provide to bring the outdoor air stream to the prescribed post-supply setpoint conditions. It is defined as:

$$\mathrm{CL} = \dot{m}_{SUP}\left(h_{ODA} - h_{set}\right) \tag{21}$$

where the setpoint enthalpy h_{set} is evaluated at the post-supply temperature setpoint T_{set}, using the humidity ratio of the extract air stream. The humidity ratio used is limited by the saturation humidity ratio at T_{set} to ensure physically consistent conditions. It is important to note that the CL is a derived parameter serving strictly as a compact comparative metric, as the experimental test matrix was defined by controlling the outdoor temperature, airflow rate, and post-supply setpoint, rather than through a controlled sweep of the load itself.

5. Results and discussion

In this section, the developed model is first compared against the acquired experimental data. Subsequently, a comprehensive performance analysis is conducted to evaluate the system in its standard configuration against the proposed architectural alternatives.

5.1. Model validation

Focusing initially on the ventilation unit subsystem, the deviations between simulated and measured thermo-hygrometric conditions at the unit outlets (i.e., *SUP* and *EHA*) are presented in Figs. 9 and 10. No calibration procedure was applied to compensate for potential inaccuracies in the heat and mass transfer modeling. For the ERV unit, convective heat-transfer coefficients (and the corresponding mass-transfer coefficients) were estimated using the correlation of Muzychka–Yovanovich under the uniform wall temerature (UWT) hypothesis [29]. This specific formulation was adopted because it yielded closer agreement with the experimental data compared to the correlations based on the uniform wall flux (UWF) hypothesis, a finding consistent with the literature [38].

On the other end, for the HRV unit, the Muzychka–Yovanovich correlations under UWF assumption yielded a better match with the experimental data. This result can be explained by the structural characteristics of the exchanger under consideration, which features a thicker

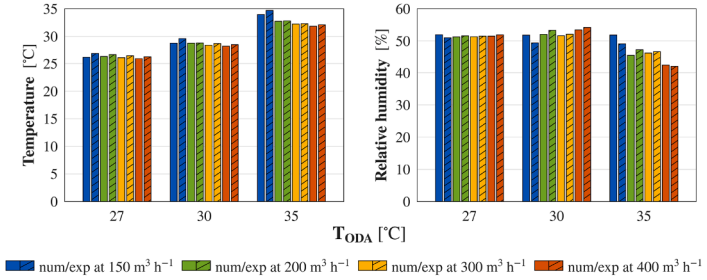

(a) SUP side

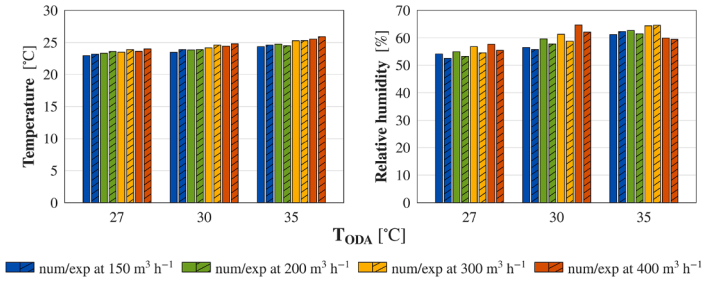

(b) EHA side

Fig. 9. Relative error for temperature and relative humidity of the MVHR/ERV unit.

Table 5
Mean Absolute Error (MAE) and Root Mean Square Error (RMSE) for MVHR/ERV air outlet conditions.

	T_{SUP} [°C]	RH_{SUP} [%]	T_{EHA} [°C]	RH_{EHA} [%]
MAE	0.3	1.6	0.4	1.0
RMSE	0.3	1.8	0.4	1.3

Table 6
MAE and RMSE for MVHR/HRV air outlet conditions.

	T_{SUP} [°C]	RH_{SUP} [%]	T_{EHA} [°C]	RH_{EHA} [%]
MAE	0.3	1.4	0.8	1.4
RMSE	0.4	2.0	0.8	1.6

Table 7
MAE and RMSE for performance indicators and air-outlet conditions of the MFRBV/ERV unit.

	T_{PSUP} [°C]	RH_{PSUP} [%]	T_{PEHA} [°C]	RH_{PEHA} [%]	$\dot{Q}_{sys}$ [W]	EER_{sys} [-]
MAE	0.8	4.8	1.7	0.9	68	0.3
RMSE	0.9	6.0	1.9	1.1	86	0.4

Table 8
MAE and RMSE for refrigerant side temperature control variables.

	T_{evap} [°C]	T_{cond} [°C]	T_{dis} [°C]
MAE	1.2	1.6	3.3
RMSE	1.3	1.8	4.5

separating wall, a channel aspect ratio close to unity, and a wall material with low thermal conductivity. These aspects make the uniform wall-flux assumption more physically consistent.

Overall, the MVHR model demonstrates strong predictive capabilities across all tested conditions. As detailed in Table 5, the Mean Absolute Error (MAE) for the ERV case is restricted to 0.4°C for temperature and 1.6% for relative humidity; similarly, the HRV case (Table 6) exhibits comparable accuracy with maximum MAEs of 0.8°C and 1.4%, respectively. In addition to these low mean absolute errors, the consistently low Root Mean Square Error (RMSE) values across all test cases confirm the absence of significant local outliers.

Following the successful validation of the isolated ventilation unit model, the analysis is then expanded to encompass the complete system. For the comprehensive validation of the overall unit, the deviations in the outlet air conditions, corresponding to the thermo-hygrometric states of the PSUP and PEHA streams, are shown in Figs. 11 and 12. Furthermore, deviations in the total cooling capacity ($\dot{Q}_{sys}$) and overall energy efficiency ratio (EER_{sys}) are reported in Fig. 13. Finally, the deviations for the refrigerant-cycle temperature control variables—specifically condensation, evaporation, and discharge temperatures—are presented in Fig. 14.

Overall, the system-level model exhibits strong agreement with the experimental data across the full range of tested conditions, yielding global performance indicators that consistently fall within a ±10% accuracy band. A quantitative assessment through statistical metrics further confirms the reliability of the developed model: the Mean Absolute Error (MAE) for the post-supply and post-exhaust air outlet temperatures (T_{PSUP} and T_{PEHA}) remains strictly below 1.7°C, with corresponding Root Mean Square Errors (RMSE) not exceeding 1.9°C. Similarly, integral metrics, including the system capacity ($\dot{Q}_{sys}$) and energy efficiency ratio (EER_{sys}), achieve notably low MAEs of 68 W and 0.3, respectively (Table 7).

Refrigerant-side control variables also align closely with empirical trends, showing an RMSE of approximately 1.8°C for both evaporation and condensation temperatures. While the discharge temperature exhibits a marginally higher MAE of 3.3°C, it stays entirely within an acceptable tolerance for macroscopic simulations. Consequently, this high degree of consistency confirms that the developed model accurately captures the dominant physical phenomena, establishing it as a reliable predictive tool (Table 8).

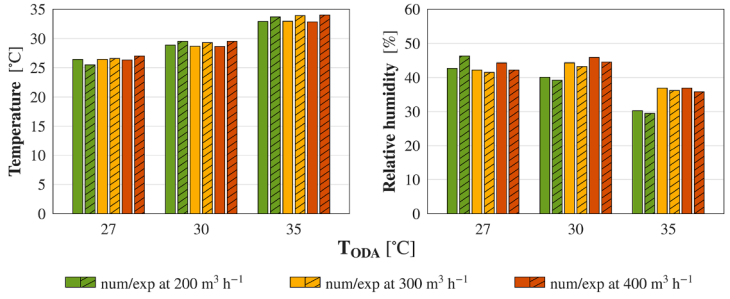

(a) SUP side

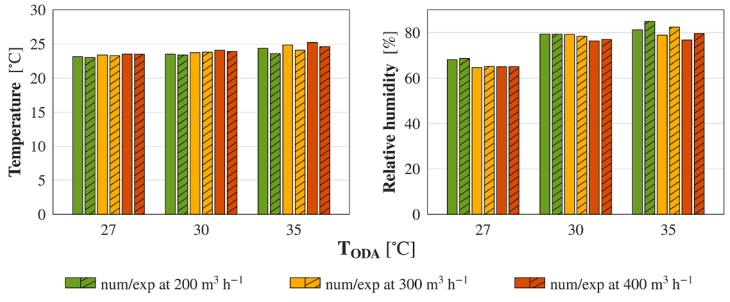

(b) EHA side

Fig. 10. Relative error for temperature and relative humidity of the MVHR/HRV unit.

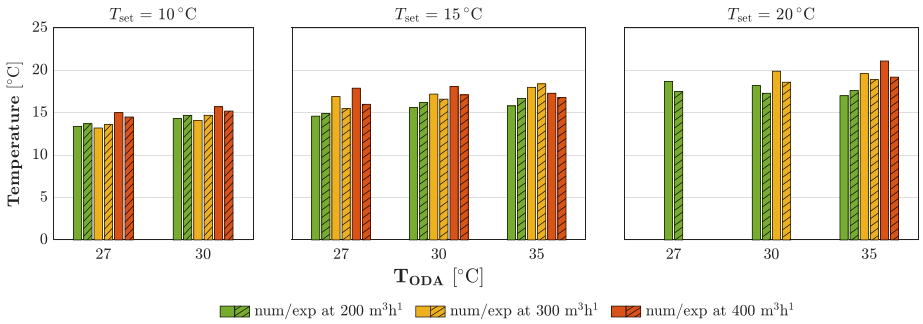

(a) Temperature

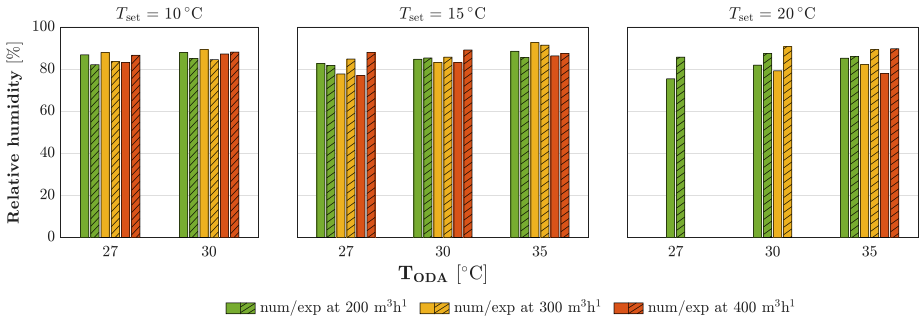

(b) Relative humidity

Fig. 11. Deviations of air outlet conditions for the MFRBV/ERV unit PSUP side.

5.2. Performance analysis

The predictive capability of the developed model was exploited to address the research questions introduced in Section 1. Two different series of analyses were carried out. The first focused on the fixed-frequency operation of the compressor. Here, the boundary conditions of the experimental campaign—including indoor and outdoor thermo-hygrometric conditions, airflow rates, and compressor speed—were replicated within the model. To ensure a fair comparison, the architectural variations (i.e., OEA loop activation, recovery core type, and bypass configurations) were evaluated directly against the standard configuration model under these identical external conditions, rather than against the raw experimental data.

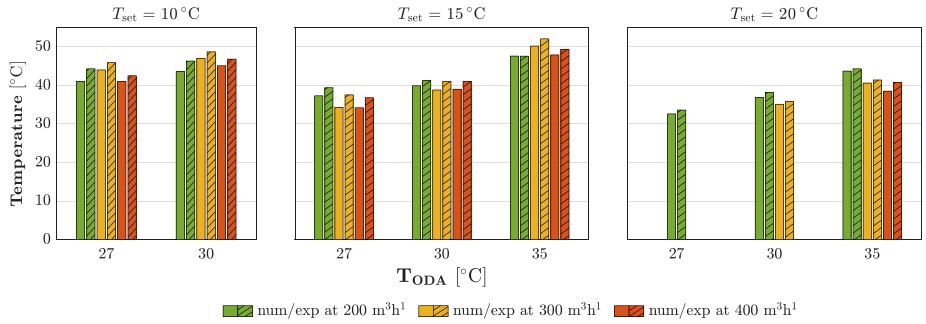

(a) Temperature

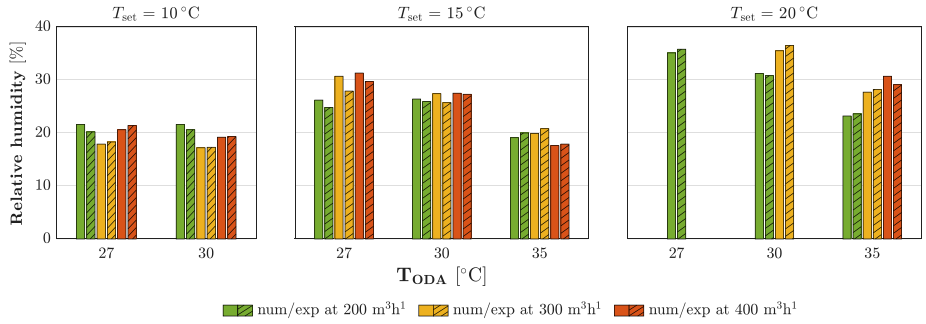

(b) Relative humidity

Fig. 12. Deviations of air outlet conditions for the MFRBV/ERV unit PEHA side.

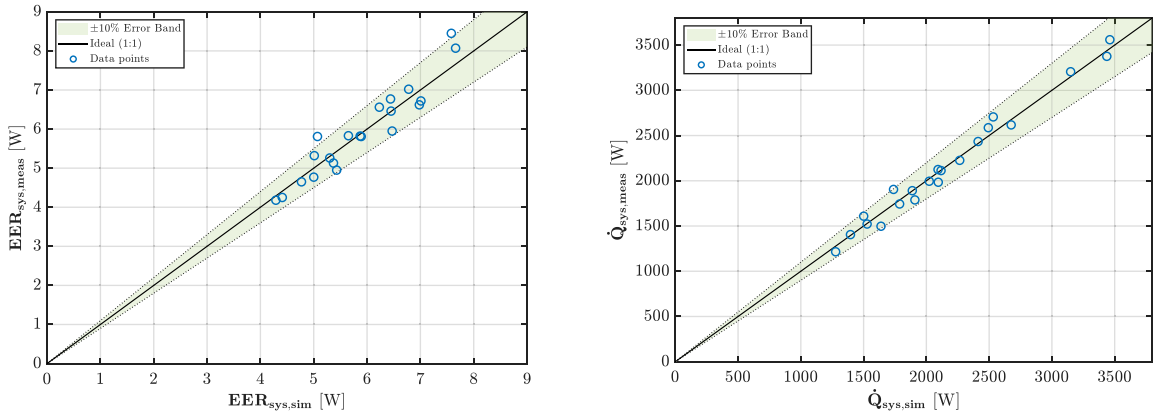

(a) System EER

(b) System capacity

Fig. 13. Deviation of performance indicators for the MFRBV/ERV unit.

In the second series, the same environmental conditions and architectural variations were maintained, but the compressor frequency was no longer fixed. Instead, the control logic of the unit was enabled, allowing the compressor speed to adjust dynamically to satisfy the post-supply temperature setpoint.

This two-step procedure provided a consistent framework: fixed-frequency tests revealed the intrinsic thermodynamic potential of each configuration, whereas control-driven tests showed how the operating condition shifted once the compressor logic governed the system response.

5.2.1. *Recirculation fan (OEA)*

The impact of introducing an auxiliary Outdoor to Exhaust Air (OEA) recirculation fan on overall system performance was examined in this section. Two configurations were compared, identical in all respects except for the inclusion of this auxiliary fan. In the modified configuration, the fan recirculates outdoor air, thereby increasing the airflow through the external heat exchanger, which acts as the condenser in summer mode. The schematic of this configuration is shown in Fig. 1. Although not part of the present experimental campaign, this solution has been implemented in practice, and both the fan geometry and performance characteristics are well established and have been incorporated into the model.

In the present analysis, the unit was assumed to operate ideally (i.e., without external ducting). Consequently, the airflow provided by the OEA fan depended solely on the internal pressure losses of the unit, which scale with the ventilation flow rate. Under the investigated conditions, the OEA fan was set to its maximum speed, corresponding to the highest achievable airflow.

Fixed-frequency analysis

The results in Fig. 16 are organized by airflow rate and outdoor tem-

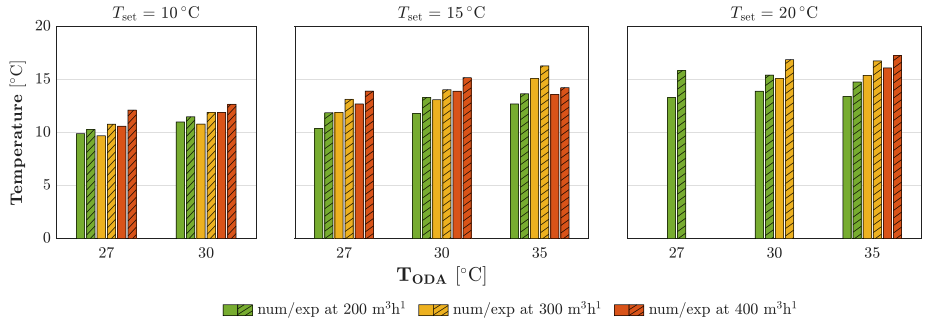

(a) Evaporation temperature

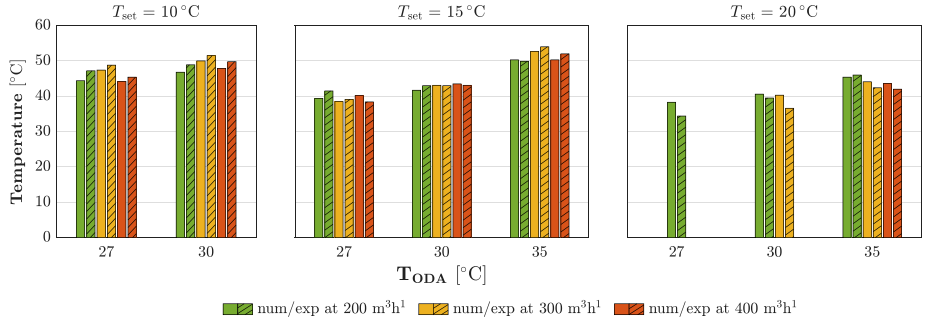

(b) Condensation temperature

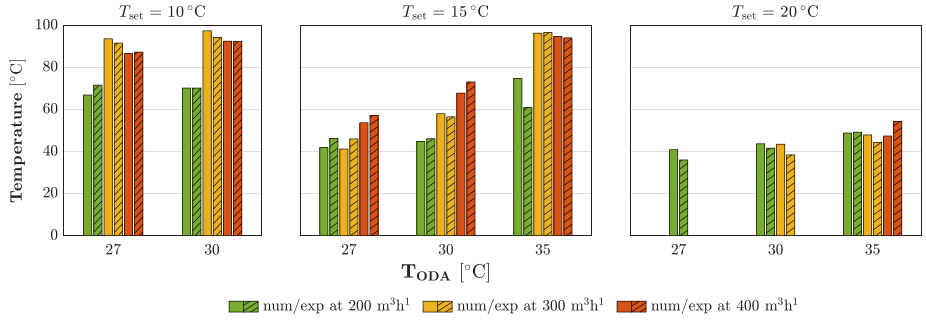

(c) Discharge temperature

Fig. 14. Deviations of refrigerant side temperature control variables for the MFRBV/ERV unit.

perature, providing a framework for interpreting the unit's behavior. Results show that, for the same cooling load, the system can follow different operating paths depending on the boundary conditions, since the maximum compressor frequency is constrained by the control logic as a function of both condenser air-inlet temperature and ventilation airflow. This safeguard prevents excessive condensation and discharge temperatures but also implies that identical loads may correspond to different admissible compressor speeds. Performance trends can therefore be consistently interpreted only within a defined set of boundary conditions (T_{ODA}, $\dot{m}_{SUP}$, T_{ETA}), highlighting the importance of a digital model that integrates the unit's control logic.

The variations in condensation and discharge temperatures are reported in Fig. 15, which compares operations with and without the OEA fan. The data highlight that, at sufficiently high refrigerant mass flow rates, corresponding to lower post-supply setpoints (e.g., T_{set} = 10°C with T_{ODA} = 27°C and 30°C, or T_{set} = 15°C with T_{ODA} = 35°C), the condenser airflow rate became the limiting factor for heat rejection. In these operating points, the additional airflow provided by the OEA fan lowered both condensation and discharge temperatures, indicating that the compressor could be driven to higher speeds to better meet the post-supply setpoint. Conversely, at lower refrigerant flow rates (corresponding to higher post-supply setpoints), the limiting factor shifted to the temperature of the air entering the condenser. As this inlet air temperature rose, the refrigerant was required to condense at a higher saturation temperature to reject the heat load. This increase in condensation temperature directly raised the compressor discharge pressure and, consequently, the power consumption.

These dynamics are further illustrated in Fig. 17, which shows the system response under fixed operating conditions. During cooling operation, outdoor-air recirculation produced only a modest reduction in post-supply temperature, yielding a limited increase in cooling capacity. The overall impact depended strongly on the cooling load relative to the boundary conditions (T_{ODA}, $\dot{m}_{SUP}$). The most relevant improvement was observed at high cooling loads and at the intermediate airflow rate ($\dot{m}_{SUP}$ = 339 kg h^{-1}): under these conditions, the additional airflow lowered the condensation temperature and reduced compressor energy demand, while the increase in cooling capacity compensated for the extra power consumption of the auxiliary fan, resulting in a net increase in system EER. At low cooling loads, by contrast, the condenser inlet temperature dominated over airflow rate; the higher inlet temperature penalized heat rejection, raised the condensation temperature, worsened cycle performance, and increased compressor power consumption, while the auxiliary fan added further electrical demand. As a result, the system EER decreased.

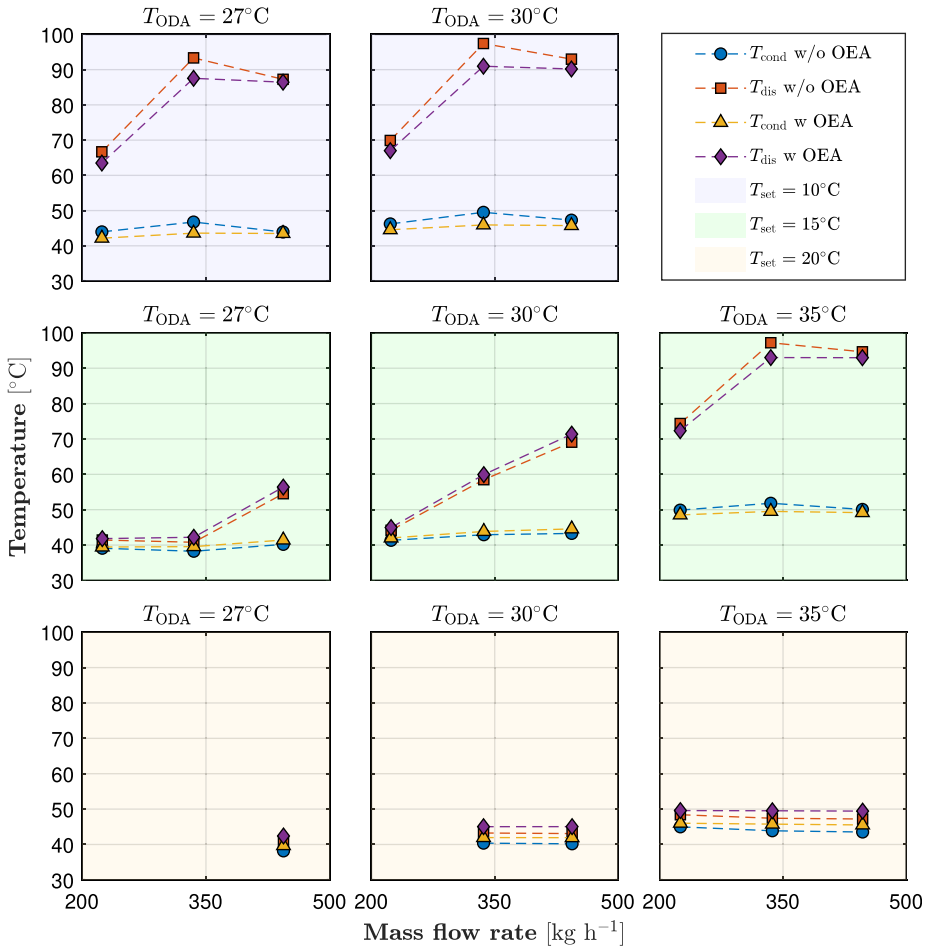

Fig. 15. Effect of OEA fan on refrigeration cycle temperatures on the high pressure side at fixed compressor frequencies.

Overall, the results suggest that auxiliary airflow is advantageous mainly at high cooling loads, where it reduces condensation and discharge temperatures and allows the compressor to operate safely at higher frequencies.

Control-driven analysis

The analysis with the compressor frequency governed by the unit's internal control logic provides further insight into the role of the auxiliary OEA recirculation fan. As shown in Fig. 16, at high cooling loads the baseline unit capacity was sometimes insufficient to meet the setpoint. In these cases, activating the auxiliary fan enabled higher compressor speeds by keeping condensation and discharge temperatures under control, thus increasing cooling capacity. A smaller additional gain also resulted from the modified thermodynamic cycle. A maximum increase of 25% was recorded for the operating point characterized by the highest cooling load at $T_{ODA} = 27°C$ and $\dot{m}_{SUP} = 447\,kg\,h^{-1}$. This capacity increase, however, came at the expense of overall system efficiency. The deterioration in EER was primarily caused by the higher electrical demand of the compressor, operating at increased speeds, compounded by the auxiliary fan power consumption. Moreover, the fan increased internal air-side pressure drops, raising the power consumption of the main ventilation fans for the same airflow rate. Under the conditions yielding the maximum capacity increase, the system EER decreased by 15.6%.

At low cooling loads, when capacity tended to exceed demand, the OEA fan had a counterproductive effect: it degraded heat-pump performance and reduced the available capacity, thereby bringing the outlet temperature closer to the setpoint. Under these conditions, the auxiliary power consumption from the OEA fan, combined with the additional power required for the MVHR fans to overcome the extra pressure drop introduced by the recirculation loop, became comparable to that of the compressor, strongly penalizing the system EER.

In general, these findings suggest that auxiliary airflow can enhance cooling capacity at high loads by improving the control of condensation and discharge temperatures, thereby allowing the compressor to operate at higher frequencies, but it can reduce overall system efficiency, especially under partial-load conditions.

5.2.2. *Enthalpy recovery vs heat recovery*

The impact of the recovery strategy on system-level performance was evaluated by coupling the system with two identically sized, quasi-counter-flow heat recovery cores: (i) a sensible heat-recovery core (HRV-type) with polymer plates and square channels, and (ii) an enthalpy-recovery core (ERV-type) with a membrane and rectangular channels. As shown in Fig. 18(a) and (b), the HRV unit supplied cooler but more humid air, whereas the ERV unit delivered warmer but drier air. These contrasting outlet conditions defined the boundary states of the coupled heat pump unit and influenced the overall system performance.

The cycle-level analysis at fixed compressor speed showed that the HRV configuration (EAHP/HRV) operated with higher evaporating and condensing temperatures respect to the ERV configuration (EAHP/ERV). The higher dew point of the supply air led to earlier water condensation on the coil and increased the evaporating pressure, while the stronger sensible recovery raised the condenser temperature (see Fig. 19(a)). As illustrated in Fig. 19(b), the gain in evaporating temperature dominated, resulting in consistently higher internal Carnot efficiency for the EAHP/HRV configuration. However, this

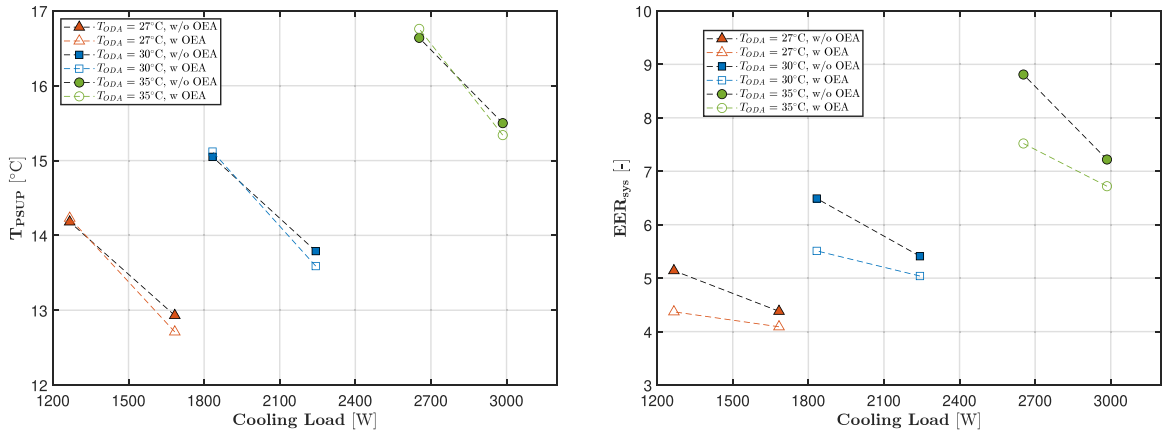

(a) Results at $\dot{m}_{SUP}$ = 227 kg h^{-1}, $\dot{m}_{PEHA}$ = 565 kg h^{-1}

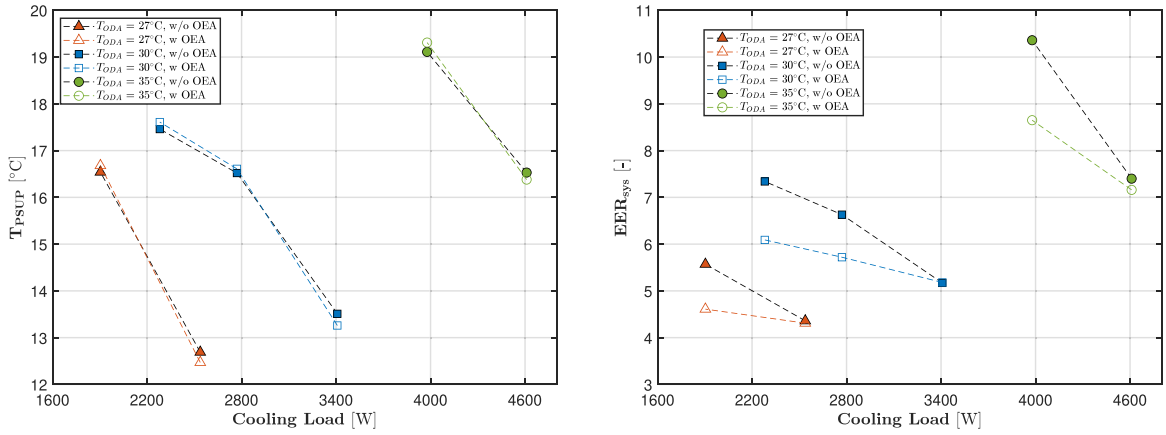

(b) Results at $\dot{m}_{SUP}$ = 339 kg h^{-1}, $\dot{m}_{PEHA}$ = 650 kg h^{-1}

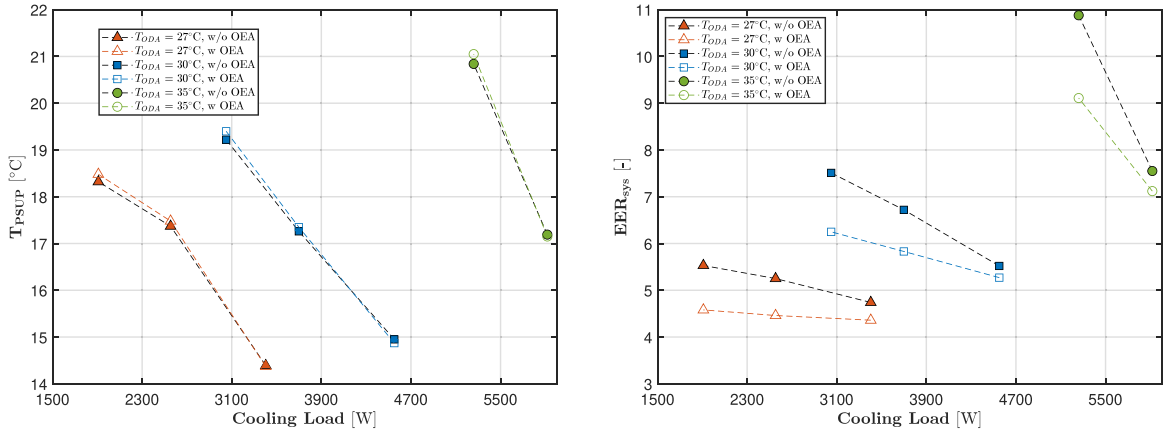

(c) Results at $\dot{m}_{SUP}$ = 447 kg h^{-1}, $\dot{m}_{PEHA}$ = 724 kg h^{-1}

Fig. 16. Post supply temperature and overall EER of the standard MFRBV unit and the alternative MFRBV unit at fixed compressor frequency.

thermodynamic improvement did not translate into a tangible benefit at the system-level. Conversely, as demonstrated in Fig. 20, the EAHP/ERV configuration achieved lower post-supply temperatures and higher system EER. The HRV unit delivered colder but more humid air, forcing the heat pump to allocate a larger share of its capacity to latent cooling, whereas the ERV unit transferred part of this load through the membrane, leaving more sensible capacity for temperature reduction. An average of 28% greater cooling capacity and 25% higher EER for the EAHP/ERV system, relative to the EAHP/HRV system, was recorded. With active compressor control (not shown here for brevity), the ERV advantage became even more pronounced, since the EAHP/HRV system had to operate at higher compressor speeds to reach the same temperature setpoints, leading to a further decrease in system EER.

In summary, while the system coupled with the HRV unit improves the theoretical cycle efficiency of the HP, the system equipped with the ERV provides lower post-supply temperatures and higher overall EER, making it the preferable configuration under summer conditions.

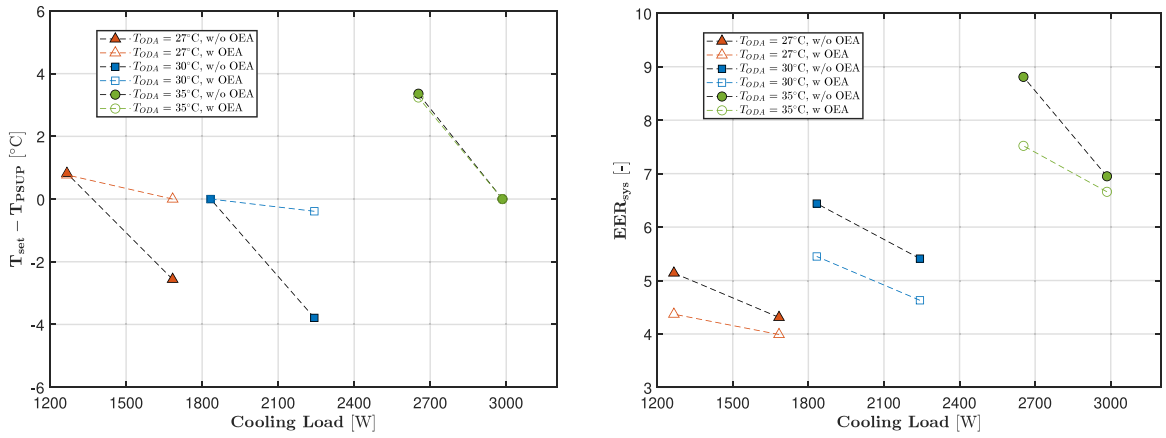

(a) Results at $\dot{m}_{SUP}$ = 227 kg h^{-1}, $\dot{m}_{PEHA}$ = 565 kg h^{-1}

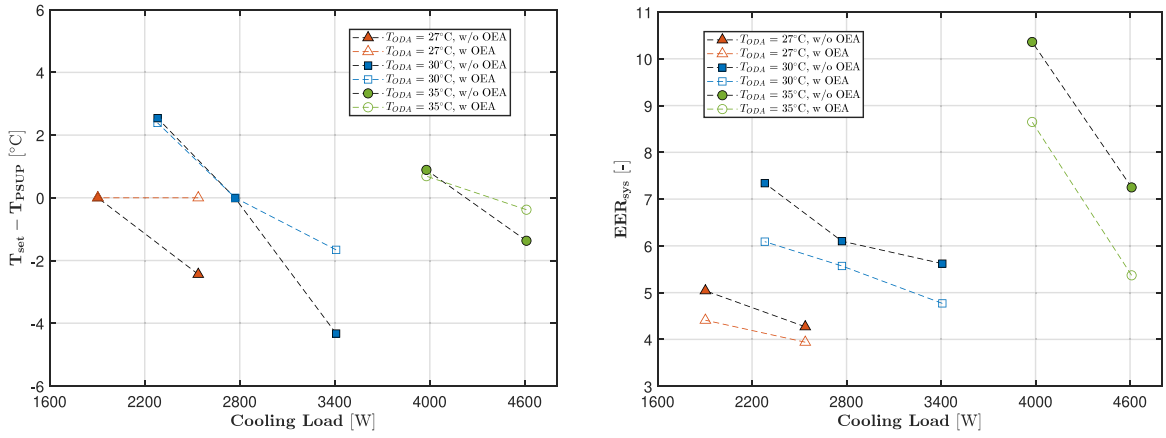

(b) Results at $\dot{m}_{SUP}$ = 339 kg h^{-1}, $\dot{m}_{PEHA}$ = 650 kg h^{-1}

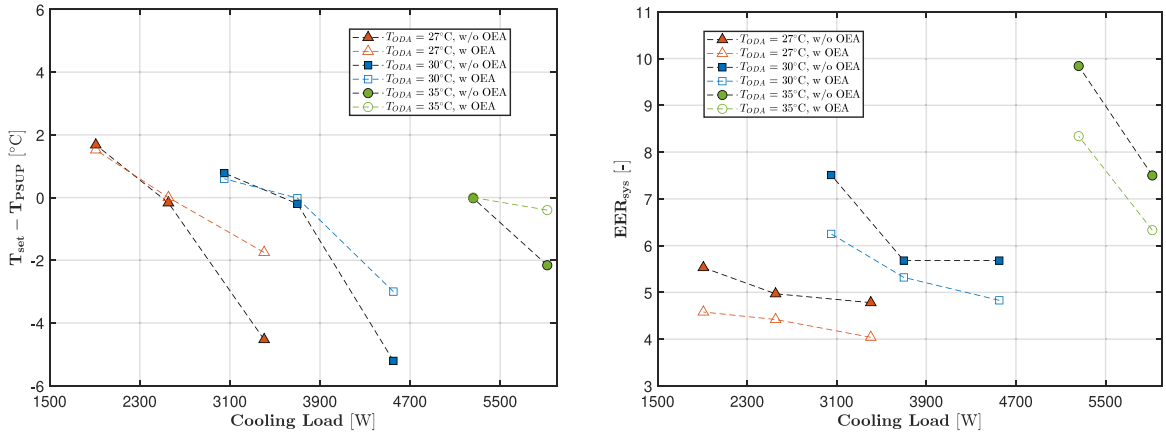

(c) Results at $\dot{m}_{SUP}$ = 447 kg h^{-1}, $\dot{m}_{PEHA}$ = 724 kg h^{-1}

Fig. 17. Post supply temperature and overall EER of the standard MFRBV unit and the alternative MFRBV unit.

5.2.3. Bypass of the recovery exchanger

Fixed-frequency analysis

The digital model was used to assess the impact of different bypass levels of the recovery exchanger on the coupled ventilation–heat pump system. The hypothesis was that increasing the bypass fraction would yield more favorable inlet conditions for the heat pump (higher evaporating and lower condensing temperatures), potentially raising cycle EER, but at the cost of losing the pre-conditioning effect of heat/energy recovery.

Four bypass configurations were simulated: 0%, 30%, 50%, and 100% of the airflow bypassing the recovery exchanger. The 100% bypass case represented a limiting scenario, effectively corresponding to a system coupled with a ventilation unit without heat/enthalpy recovery. The analysis was conducted for both ERV- and HRV-based systems.

The results (Figs. 21 and 22) confirmed that the heat pump EER increased with bypass opening fraction, reaching its maximum when the exchanger was fully bypassed (Fig. 21(b)). However, at

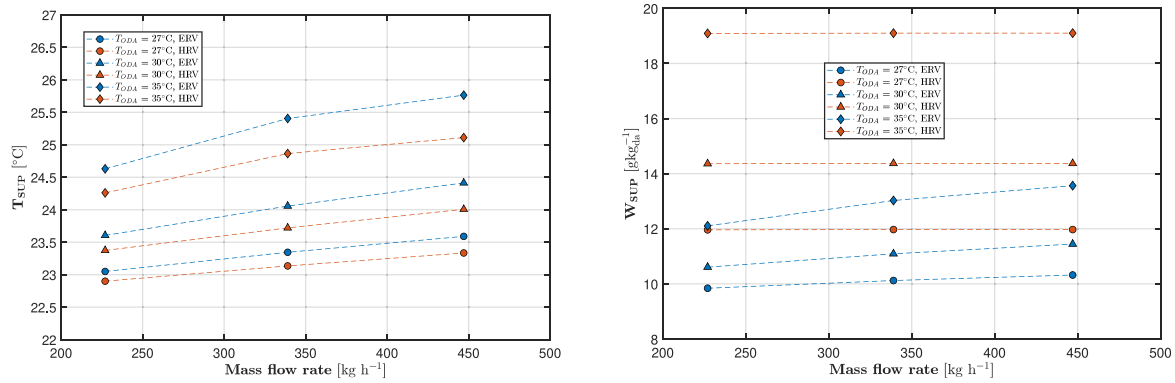

(a) Supply air temperature

(b) Supply air humidity ratio

Fig. 18. Impact of the recovery strategy on MVHR air outlet conditions.

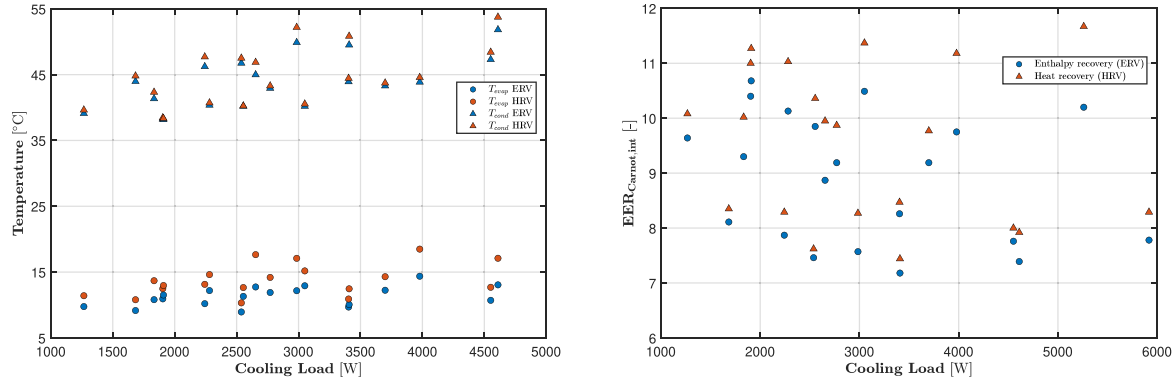

(a) Evaporation and condensation temperatures

(b) Internal Carnot EER

Fig. 19. Impact of the recovery strategy on the refrigeration cycle at fixed compressor frequencies.

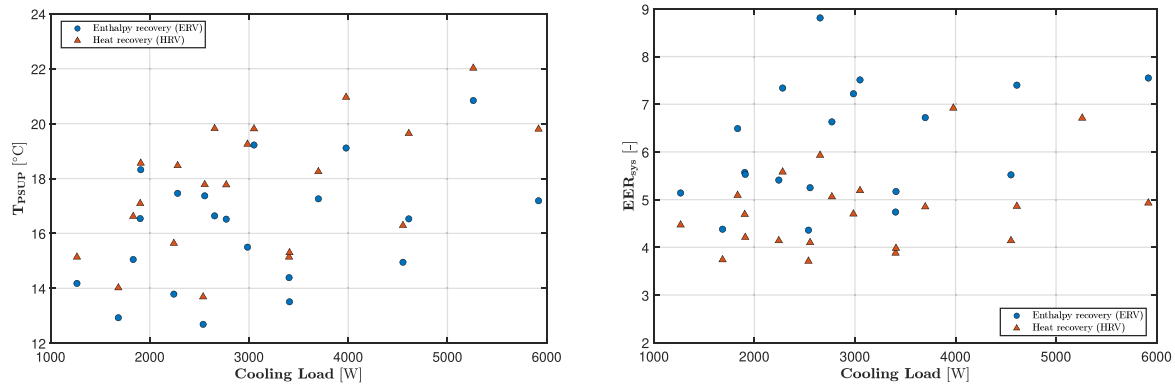

(a)

(b)

Fig. 20. Post-supply temperature (a) and overall EER (b) at fixed compressor frequencies.

the system-level, the overall performance deteriorated consistently, as the loss of heat recovery outweighed the modest gains in cycle efficiency.

The post-supply temperature profiles indicated a progressive reduction in sensible cooling capacity with increasing bypass, particularly for the ERV, highlighting the role of latent recovery in alleviating the evaporator load.

Overall, exchanger bypass during summer conditions does not improve system efficiency and should be limited to specific cases such as free-cooling. The analysis underscores the importance of evaluating strategies at the system-level, as subsystem benefits may not translate into overall improvements.

Control-driven analysis

The same bypass analysis was repeated with the compressor frequency governed by the unit's internal control logic, instead of being fixed at prescribed values. The corresponding results are presented in Figs. 23 and 24. As in the fixed-frequency case, a general decrease in system performance was observed for both ERV- and HRV-based configurations as the bypass fraction increased, confirming the fundamental role of the recovery unit regardless of the adopted control strategy.

However, an additional effect emerged under low cooling-load conditions. In these operating regions, the heat pump tended to overshoot the post-supply temperature setpoint, as its minimum available capacity still exceeded the actual demand. Under such circumstances, bypassing

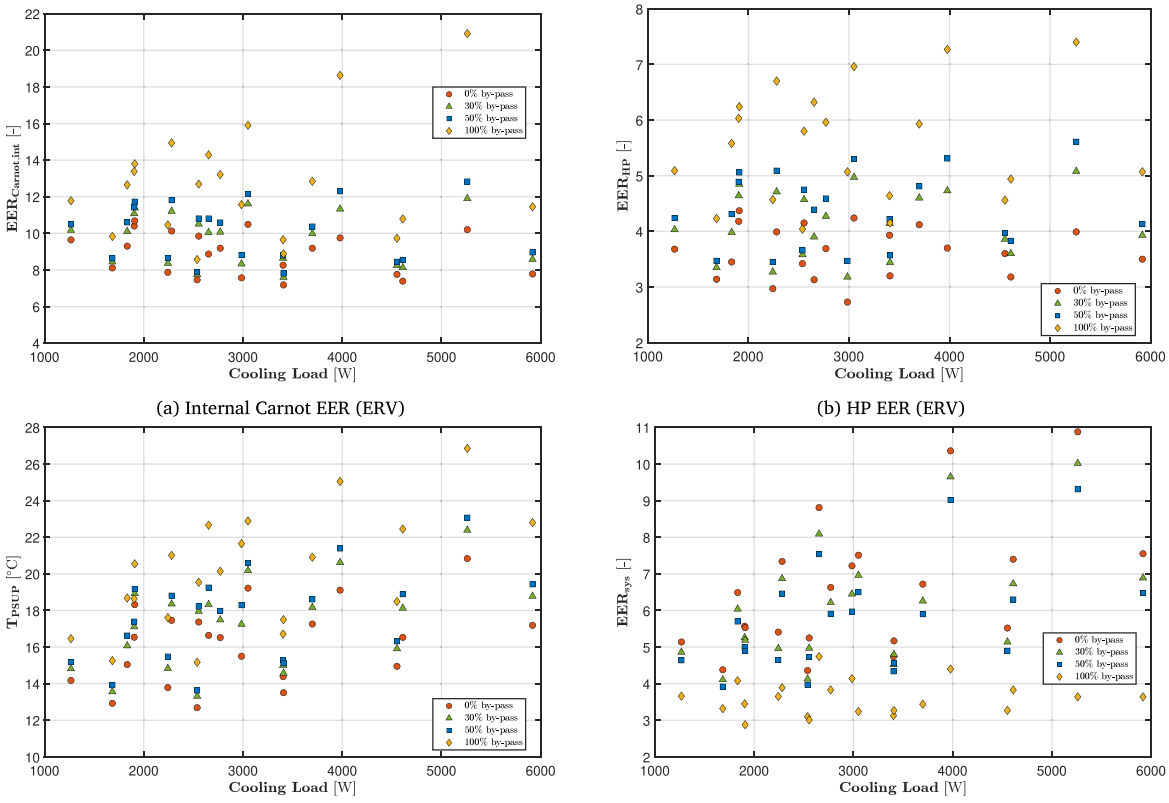

(a) Internal Carnot EER (ERV)

(b) HP EER (ERV)

(c) Post-supply temperature (ERV)

(d) System EER (ERV)

Fig. 21. Performance under different bypass levels of the enthalpy recovery exchanger (ERV).

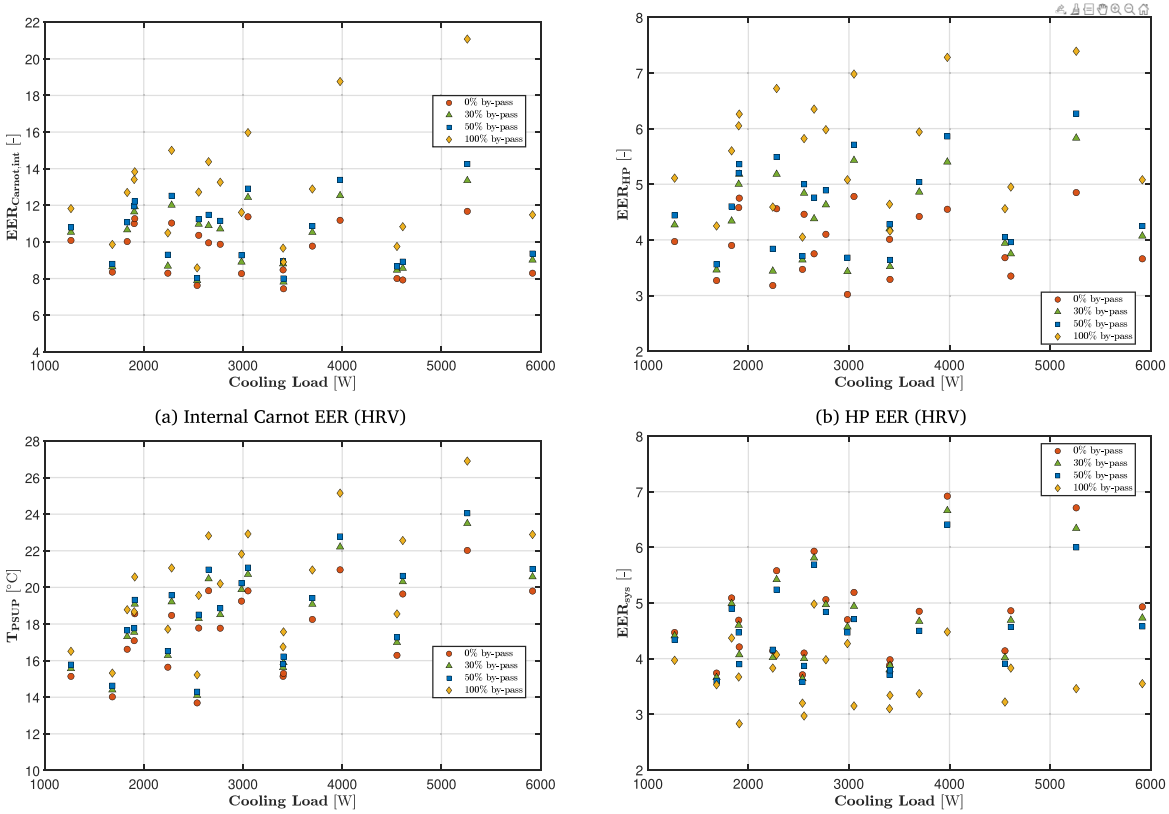

(a) Internal Carnot EER (HRV)

(b) HP EER (HRV)

(c) Post-supply temperature (HRV)

(d) System EER (HRV)

Fig. 22. Performance under different bypass levels of the heat recovery exchanger (HRV).

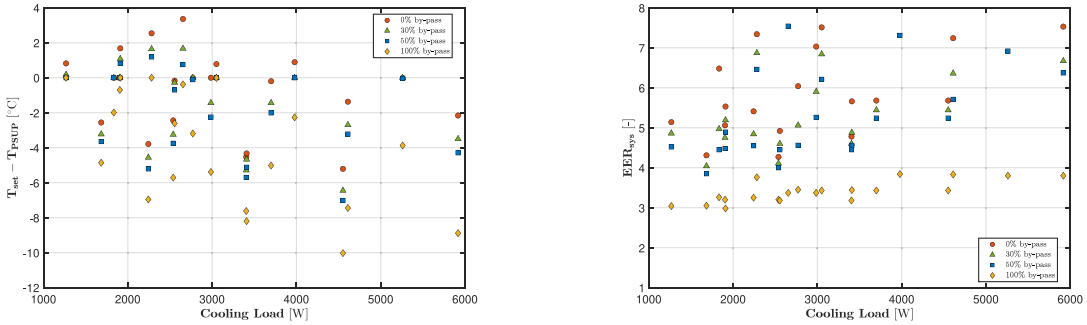

Fig. 23. Post supply temperature deviation and overall EER under different degree of bypass of the enthalpy recovery exchanger (ERV).

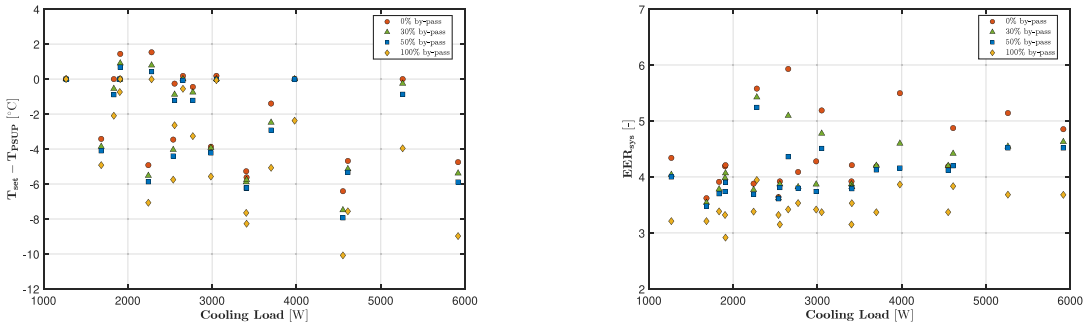

Fig. 24. Post supply temperature deviation and overall EER under different degree of bypass of the heat recovery exchanger (HRV).

the recovery exchanger modified the source and sink conditions in a way that effectively reduced the mismatch between capacity and load. As a result, the system operated closer to the desired post-supply setpoint, with a larger number of operating points showing smaller or no deviations.

This finding indicates that, at low cooling loads, bypassing the exchanger may improve the fulfillment of supply-air temperature requirements, although this occurs at the expense of a lower EER. In practice, the bypass introduces a trade-off: it reduces energy efficiency but enhances setpoint tracking under partial-load conditions where the compressor's minimum modulation is insufficient.

A conventional solution to this mismatch is on–off compressor cycling, which reduces the delivered capacity by intermittently switching the heat pump on and off. While this approach can restore setpoint tracking, it entails well-known drawbacks: frequent start–stop sequences increase mechanical wear on the compressor, cause transient inefficiencies during each restart, and may compromise thermal comfort due to the pulsed nature of capacity delivery. By contrast, exchanger bypass achieves a comparable modulation effect continuously, without imposing additional mechanical stress or introducing cycling-induced inefficiencies.

6. Conclusions

In this study, a physics-based model of a multifunctional balanced ventilation unit integrating an exhaust-air to supply-air heat pump was developed and experimentally validated. The model was tested against multiple steady-state operating points covering the full cooling operating range of the system. The comparison showed good agreement with measurements, with overall performance indicators predicted within ±10%, while the MAE and RMSE for air outlet and refrigerant conditions remained strictly within acceptable limits. This confirms its capability to serve as a reliable predictive tool, applicable beyond the specific operating range covered by the experiments.

The digital model was subsequently employed to address three questions of both practical and scientific relevance.

First, the analysis of the integration of an auxiliary outdoor-to-exhaust fan showed that the additional airflow can increase cooling capacity at high loads by allowing the compressor to operate at higher frequencies. This advantage, however, comes with a modest efficiency penalty caused by the additional electrical demand. In the most favorable case, cooling capacity increased by up to 25%, while the EER decreased by approximately 16%.

Second, the comparison between heat and enthalpy recovery indicated that the HRV unit supplies colder but more humid air than the ERV unit. At the system-level, however, this additional humidity in the configuration with the HRV increases the latent load on the heat pump. Consequently, a larger proportion of the cooling capacity is diverted to dehumidification rather than sensible cooling, resulting in higher post-supply air temperatures and a lower EER than in the configuration with the ERV unit. On average, the system equipped with the ERV unit delivered a 28% higher cooling capacity and a 25% higher EER than the system equipped with the HRV unit.

Finally, the investigation of bypassing the recovery exchanger showed that, although higher bypass opening fractions improve the efficiency of the refrigeration cycle, they significantly reduce the efficiency of the overall system. The main advantage of this strategy appears under partial-load conditions, where bypass operation emerges as a potential means to achieve smoother tracking of the post-supply setpoint compared with conventional on–off cycling.

Overall, this research demonstrates how physics-based models can extend the scope of conventional testing by enabling systematic and detailed exploration of coupled thermodynamic and internal (onboard) control phenomena. The developed framework provides both a deeper understanding of the interactions among recovery, airflow management, and compressor operation, and a robust basis for the design and optimization of next-generation multifunctional ventilation units aimed at achieving higher energy efficiency and indoor comfort in low-energy buildings.

CRediT authorship contribution statement

Roberto Sedoni: Writing – review & editing, Writing – original draft, Visualization, Validation, Software, Methodology, Investigation, Formal analysis, Data curation, Conceptualization; **Marco Romani:** Supervision, Resources, Methodology, Funding acquisition, Conceptualization; **William Monteleone:** Writing – review & editing, Writing – original draft, Visualization, Supervision, Software, Methodology, Investigation, Data curation; **Fabian Ochs:** Writing – review & editing, Supervision, Resources, Project administration, Formal analysis; **Diego Angeli:** Writing – review & editing, Visualization, Supervision, Project administration, Methodology, Funding acquisition, Conceptualization; **Paolo E. Santangelo:** Writing – review & editing, Supervision, Methodology, Formal analysis, Conceptualization.

Declaration of competing interest

The authors declare that they have no known competing financial interests or personal relationships that could have appeared to influence the work reported in this paper.

Acknowledgments

We express our gratitude to the Zehnder Group - Competence Center Campogalliano (MO) and to our colleagues of the University of Innsbruck for their assistance and the allocation of necessary resources throughout this research endeavor.

Data availability

Data will be made available on request.

References

[1] M. Mannan, S.G. Al-Ghamdi, Indoor air quality in buildings: a comprehensive review on the factors influencing air pollution in residential and commercial structure, Int. J. Environ. Res. Public Health 18 (6) (2021). https://doi.org/10.3390/ijerph18063276
[2] R. Sedoni, M. Romani, P.E. Santangelo, A hybrid model for the assessment of indoor environmental quality in buildings: an insight into mold growth, Energy Rep. 13 (2025) 4114–4125. https://doi.org/10.1016/j.egyr.2025.03.037
[3] A. Tejani, R. Khandelwal, Enhancing indoor air quality through innovative ventilation designs: a study of contemporary HVAC solutions, ESP Int. J. Adv. Sci. Technol. 1 (2) (2023) 35–48. https://doi.org/10.56472/25839233/IJAST-V1I2P106
[4] Passive House Institute, Criteria for the passive house, EnerPHit and PHI low energy building standard, 2016. https://passipedia.org/_media/picopen/9f_160815_phi_building_criteria_en.pdf
[5] G. Murano, F. Caffari, N. Calabrese, Energy potential of existing reversible air-to-air heat pumps for residential heating, Sustainability 16 (14) (2024). https://doi.org/10.3390/su16146047
[6] O. Eguiarte, A. Garrido-Marijuán, P. de Agustín-Camacho, L. del Portillo, A. Romero-Amorrortu, Energy, environmental and economic analysis of air-to-air heat pumps as an alternative to heating electrification in Europe, Energies 13 (15) (2020) 3939. https://doi.org/10.3390/en13153939
[7] A. Shirani, A. Merzkirch, J. Roesler, S. Leyer, F. Scholzen, S. Maas, Experimental and analytical evaluation of exhaust air heat pumps in ventilation-based heating systems, J. Build. Eng. 44 (2021) 102638. https://doi.org/10.1016/j.jobe.2021.102638
[8] D. Siegele, F. Ochs, W. Feist, Novel speed-controlled exhaust-air to supply-air heat pump combined with a ventilation system, Appl. Therm. Eng. 162 (2019) 114230. https://doi.org/10.1016/j.applthermaleng.2019.114230
[9] W. Li, J. Wang, W. Shi, J. Lu, High-efficiency cooling solution for exhaust air heat pump: modeling and experimental validation, Energy 254 (2022) 124396. https://doi.org/10.1016/j.energy.2022.124396
[10] X. Cao, C. Yang, Z. Sun, Y.-M. Lu, M.-M. Chang, L.-L. Shao, C.-L. Zhang, A novel packaged outdoor air dehumidifier with exhaust air heat pump - experiment and simulation, Appl. Therm. Eng. 181 (2020) 115986. https://doi.org/10.1016/j.applthermaleng.2020.115986
[11] C.-H. Liang, L.-Z. Zhang, L.-X. Pei, Performance analysis of a direct expansion air dehumidification system combined with membrane-based total heat recovery, Energy 35 (9) (2010) 3891–3901. https://doi.org/10.1016/j.energy.2010.06.002
[12] Z.-Y. Zhang, C.-L. Zhang, M.-C. Ge, Y. Yu, A frost-free dedicated outdoor air system with exhaust air heat recovery, Appl. Therm. Eng. 128 (2018) 1041–1050. https://doi.org/10.1016/j.applthermaleng.2017.09.091
[13] X. Li, G. Ma, L. Wang, S. Xu, L. Gao, J. Wu, Performance analysis of a fresh air and indoor air co-treatment parallel-loop exhaust air heat pump for buildings, J. Build. Eng. 96 (2024) 110414. https://doi.org/10.1016/j.jobe.2024.110414
[14] X. Jia, G. Ma, F. Zhou, S. Liu, G. Wu, Q. Sui, Experimental study and operation optimization of a parallel-loop heat pump for exhaust air recovery in residential buildings, J. Build. Eng. 45 (2022) 103468. https://doi.org/10.1016/j.jobe.2021.103468
[15] M. Thalfeldt, J. Kurnitski, E. Latõšov, Exhaust air heat pump connection schemes and balanced heat recovery ventilation effect on district heat energy use and return temperature, Appl. Therm. Eng. 128 (2018) 402–414. https://doi.org/10.1016/j.applthermaleng.2017.09.033
[16] H.A. Sikder, T. Tasnim, E. Haque, D. Sarker, Harvesting rejected heat by the split A/C condenser for producing warm water, IUBAT Rev. 7 (2) (2024) 44–63. https://doi.org/10.3329/iubatr.v7i2.78797
[17] B. Guo, X. Huang, Q. Li, Y. Fan, Y. Yang, Y. Wang, J. He, A complete ASHP-based HVAC hybrid model for building energy retrofits via two-stage event-triggered model predictive control, J. Build. Eng. 100 (2025) 111624. https://doi.org/10.1016/j.jobe.2024.111624
[18] L. Tang, H. Xie, Y. Wang, Z. Xu, Deeply flexible commercial building HVAC system control: a physics-aware deep learning-embedded MPC approach, Appl. Energy 388 (2025) 125631. https://doi.org/10.1016/j.apenergy.2025.125631
[19] Q. Si, J. Wei, Y. Li, H. Cai, Optimization for the model predictive control of building hvac system and experimental verification, Buildings 12 (10) (2022) 1602. https://doi.org/10.3390/buildings12101602
[20] A.C. Ispir, G.O. Rodriguez, W. De Vries, M. Speetjens, Digital twin development of a full-scale industrial heat pump, Appl. Therm. Eng. 269 (2025) 125921. https://doi.org/10.1016/j.applthermaleng.2025.125921
[21] P. Li, D. Vrabie, D. Li, S.C. Bengea, S. Mijanovic, Z.D. O'Neill, Simulation and experimental demonstration of model predictive control in a building HVAC system, Sci. Technol. Built Environ. 21 (6) (2015) 721–732. https://doi.org/10.1080/23744731.2015.1061888
[22] European Committee for Standardization (CEN), EN 16573:2017 Ventilation for buildings — Performance testing of components/products for residential buildings — Multifunctional balanced ventilation units for single family dwellings, including heat pumps, European Standard, 2017.
[23] R. Sedoni, Research data and files for the paper "Comprehensive modelling and experimental analysis of exhaust air heat pumps for residential applications under cooling operation", 2026, https://git.unimore.it/225791/research-data-eahp_cooling. Repository GitLab.
[24] Documentation, Simulink, Simulation and model-based design, 2024. https://www.mathworks.com/products/simulink.html.
[25] R. Sedoni, P.E. Santangelo, D. Angeli, An accurate low-order model of a fin-and-tube heat exchanger for the dynamic simulation of heat pumps, Results Eng. (2026) 113465. . https://doi.org/10.1016/j.rineng.2026.113465
[26] MathWorks, Simscape documentation, 2025. Accessed: October 20, 2025, https://www.mathworks.com/help/simscape/.
[27] A.F. Handbook, ASHRAE fundamentals handbook, 1997.
[28] Y. Men, X. Liu, T. Zhang, Experimental and numerical analysis on heat and moisture recovery performance of enthalpy wheel with condensation, Energy Convers. Manag. 246 (2021) 114683. https://doi.org/10.1016/j.enconman.2021.114683
[29] Y.S. Muzychka, M.M. Yovanovich, Laminar forced convection heat transfer in the combined entry region of non-circular ducts, ASME J. Heat Mass Transf. 126 (1) (2004) 54–61. https://doi.org/10.1115/1.1643752
[30] L.-Z. Zhang, C.-H. Liang, L.-X. Pei, Conjugate heat and mass transfer in membrane-formed channels in all entry regions, Int. J. Heat Mass Transf. 53 (5-6) (2010) 815–824. https://doi.org/10.1016/j.ijheatmasstransfer.2009.11.043
[31] J. Min, T. Hu, X. Liu, Evaluation of moisture diffusivities in various membranes, J. Membr. Sci. 357 (1-2) (2010) 185–191. https://doi.org/10.1016/j.memsci.2010.04.019
[32] K. Križo, A. Kapjor, M. Holubčík, Polymer membranes for enthalpy exchangers, Energies 15 (16) (2022) 6021. https://doi.org/10.3390/en15166021
[33] L.-Z. Zhang, C.-H. Liang, L.-X. Pei, Heat and moisture transfer in application scale parallel-plates enthalpy exchangers with novel membrane materials, J. Membr. Sci. 325 (2) (2008) 672–682. https://doi.org/10.1016/j.memsci.2008.08.041
[34] I.R. Abadi, B. Aminian, R. Huizing, S. Rogak, S. Green, Orientation dependent permeability in asymmetric composite membranes, J. Membr. Sci. 652 (2022) 120474. https://doi.org/10.1016/j.memsci.2022.120474
[35] J.W. Mitchell, J.E. Braun, Principles of Heating, Ventilation, and Air Conditioning in Buildings, John Wiley & Sons, 2012.
[36] D. Siegele, F. Ochs, Effectiveness of a membrane enthalpy heat exchanger, Appl. Therm. Eng. 160 (2019) 114005. https://doi.org/10.1016/j.applthermaleng.2019.114005
[37] Air-Conditioning, Heating, and Refrigeration Institute, AHRI 540 (SI/I-P): Performance Rating of Positive Displacement Refrigerant Compressors and Compressor Units, Standard, AHRI, 2015.
[38] L.-Z. Zhang, Heat and mass transfer in a cross-flow membrane-based enthalpy exchanger under naturally formed boundary conditions, Int. J. Heat Mass Transf. 50 (1-2) (2007) 151–162. https://doi.org/10.1016/j.ijheatmasstransfer.2006.06.025